Working memory signals in early visual cortex do not depend on visual imagery

Simon Weber[1,2,3,*], Thomas Christophel[1,4], Kai Görgen[1,3],

Joram Soch[1,5,6], John-Dylan Haynes[1,2,3,4,7]

[1]Bernstein Center for Computational Neuroscience Berlin and Berlin Center for Advanced Neuroimaging, Charité Universitätsmedizin Berlin, corporate member of the Freie Universität Berlin, Humboldt-Universität zu Berlin, and Berlin Institute of Health, Charitéplatz 1, 10117 Berlin, Germany
[2]Research Training Group "Extrospection" and Berlin School of Mind and Brain, Humboldt-Universität zu Berlin, Luisenstraße 56, 10117 Berlin, Germany
[3]Research Cluster of Excellence "Science of Intelligence", Technische Universität Berlin, Berlin, Germany
[4]Department of Psychology, Humboldt-Universität zu Berlin, Under den Linden 6, 10117 Berlin, Germany
[5]Developmental Cognitive Neuroscience, Max Planck Institute for Human Cognitive and Brain Sciences, Stephanstraße 1a, 04103 Leipzig, Germany
[6]German Center for Neurodegenerative Diseases (DZNE), Von-Siebold-Straße 3A, 37075 Göttingen, Germany
[7]Collaborative Research Center "Volition and Cognitive Control", Technische Universität Dresden, Zellescher Weg 16, 01069 Dresden, Germany
[*]Correspondence: sweber@bccn-berlin.de

Abstract

It has been suggested that visual images are memorized across brief periods of time by vividly imagining them as if they still were there. In line with this, the contents of both working memory and visual imagery are known to be encoded already in early visual cortex. If these signals in early visual areas were indeed to reflect a combined imagery and memory code, one would predict them to be weaker for individuals with reduced visual imagery vividness. Here, we systematically investigated this question in two groups of participants. Strong and weak imagers were asked to remember images across brief delay periods. We were able to reliably reconstruct the memorized stimuli from early visual cortex during the delay. Importantly, in contrast to the prediction, the quality of reconstruction was equally accurate for both strong and weak imagers. The decodable information also closely reflected behavioral precision in both groups, suggesting it could contribute to behavioral performance, even in the extreme case of completely aphantasic individuals. Our data thus suggest that working memory signals in early visual cortex can be present even in the (near) absence of phenomenal imagery.

Introduction

In recent years, visual imagery, the ability to generate pictorial mental representations in the absence of external visual stimulation (Kosslyn & Thompson, 2003; Pearson & Kosslyn, 2015), has received increasing attention as a potential mechanism for supporting visual working memory (Albers et al., 2013; Tong, 2013).

Both visual imagery and visual working memory have been linked to the encoding of information in early visual cortex (Dijkstra et al., 2019; Klein et al., 2004; Kosslyn & Thompson, 2003; Lee & Baker, 2016; Serences, 2016). The sensory recruitment hypothesis of visual working memory (D'Esposito & Postle, 2015; Sreenivasan et al., 2014) posits that visual information is maintained using selective activation patterns in early visual cortex. This matches with a common view of visual imagery, where early visual areas encode detailed, perception-like mental images via top-down connections from high-level regions (Dijkstra et al., 2017; Mechelli, 2004). Encoding of contents has been reported to be similar between perception and visual working memory (Ester et al., 2009; Harrison & Tong, 2009; Lee et al., 2013; Serences et al., 2009). This similarity has also been shown to hold between perception and imagery across multiple features, including orientations (Albers et al., 2013), objects (Cichy et al., 2012; Lee et al., 2012; Ragni et al., 2020; Reddy et al., 2010), letters (Senden et al., 2019), and natural scenes (Naselaris et al., 2015). Furthermore, both visual working memory (Teng & Kravitz, 2019) and visual imagery (Pearson et al., 2008) can interfere with and bias perception of subsequent stimuli.

The similarities in cortical organization of imagery and visual working memory raise the question whether these two processes might be related or even share the same neural substrate. Indeed, it was directly shown for normal-viewing participants that visual working memory and imagery representations of orientations exhibit very similar neuronal activity patterns in early visual cortex (Albers et al., 2013) suggesting that visual working memory and visual imagery share a similar neural substrate (Tong, 2013). In this view, participants might briefly memorize visual stimuli in working memory tasks by vividly imagining them across the delay period.

However, the ability to generate imagery as well as its vividness differ substantially across individuals (Kosslyn et al., 2001). Some people even report the complete absence of phenomenal imagery ("aphantasia"; Zeman et al., 2015; Zeman et al., 2010). Nonetheless, these differences do not appear to manifest themselves systematically in behavioral measures of memory. Rather, most studies indicate that behavioral performance in visual working memory tasks is comparable across imagery vividness levels, including the extreme case of

2

76   aphantasic individuals (Jacobs et al., 2018; Zeman et al., 2015). However, differences have
77   been reported. For example, working memory performance for strong imagers is disrupted by
78   irrelevant visual input, while weak imagers show no such distraction effect (Keogh & Pearson,
79   2014), indicating the use of distinct memorization strategies. This is supported by comparing
80   reports of strong and weak imagers. Strong imagers report to rely mostly on visual strategies
81   when solving visual working memory tasks. In contrast, weak imagers tend to report using
82   different cognitive strategies such as verbal or categorical associations (Bainbridge et al.,
83   2021; Keogh et al., 2021; Logie et al., 2011). Thus, visual imagery might to be only one of
84   several cognitive tools that can be used to solve visual working memory tasks. If this is true,
85   then weak imagers could use different representational systems for maintaining stimulus
86   features other than sensory recruitment in early visual cortex.

88   In line with this, the cognitive-strategies framework of working memory (Pearson & Keogh,
89   2019) postulates that the cognitive strategy used to solve a working memory task determines
90   the format in which a stimulus is represented in the brain, and consequently influences how
91   much information about the stimulus is present within a given cortical region. In the case of
92   visual imagery, this could mean that individuals with high imagery vividness spontaneously
93   recruit their early visual cortex to maintain detailed stimulus representations, while individuals
94   with low imagery vividness employ alternative, non-visual strategies to solve the same
95   cognitive task. Together, this predicts that strong imagers should retain more information about
96   a stimulus feature in their visual cortex activity than weak imagers.

98   Here, we directly test this hypothesis by assessing the influence of imagery vividness on the
99   strength of visual working memory representations in visual cortex, using functional magnetic
100   resonance imaging (fMRI). We recruited two groups of study participants, one with very high
101   and one with very low imagery vividness scores as assessed by an established questionnaire
102   (VVIQ, Fig 1B, see Methods; Marks, 1973). In the main experiment, participants performed a
103   working memory task that involved memorizing a bright orientation stimulus across a brief
104   delay (Figure 1A). We used a brain-based decoder (periodic support vector regression; see
105   Methods) to reconstruct these orientations from brain activity patterns in early visual cortex
106   obtained during the memory delay period. If strong imagers indeed rely more on imagery
107   signals in early visual cortex to maintain the stimulus across the delay, this could lead to two
108   predictions: First, that sensory information should be represented more accurately in the early
109   visual brain signals of strong as opposed to weak imagers; second, sensory information in
110   early visual areas should also be more predictive of an individual's behavioral performance,
111   especially in strong imagers.

Results

Questionnaire data

Study participants were selected via an online version of the established Vividness of Visual Imagery Questionnaire (VVIQ, 210 respondents, Figure 1B; Marks, 1973). We recruited 20 participants each from the lower and upper quartile of the VVIQ score distribution, resulting in two experimental groups (average VVIQ score; weak: 40.75 ± 11.571; strong: 70.7 ± 3.262). After the second fMRI session, each participant repeated the VVIQ and also completed the Object Spatial Imagery Questionnaire (OSIQ; Blajenkova et al., 2006). VVIQ scores had a high test-retest reliability (r = 0.867, p < 0.001), and thus also the difference between weak and strong imagers, as defined by the recruitment scores, was stable across the study period (Figure 1C; $t_{(38)}$ = -5.086, p < 0.001, two-tailed). In line with previous studies, the OSIQ scores (Figure 1D) had a significant difference between weak and strong imagers for the visual items ($t_{(38)}$ = -3.338, p = 0.002, two-tailed), but no such difference for the spatial items ($t_{(38)}$ = 0.895, p = 0.377, two-tailed). Crucially, this pattern of OSIQ results replicates earlier findings obtained with this scale for weak and strong imagers (Bainbridge et al., 2021; Keogh & Pearson, 2018), which serves as a validation of the VVIQ scores as a recruitment measure.

Behavioral results

Figure 2A shows how accurately participants performed in the task. The figure plots the deviation between participants' judgements and the true orientations for each trial (grey bars), revealing that the responses were highly accurate. To assess this quantitatively, we fitted a computational model to the response distribution of each participant that yields estimates for behavioral precision and bias (von Mises mixture model; Figure 2A, black line; see Methods for details). Across all participants, responses were precise (precision κ_1 = 5.673 ± 2.377), with a small but significant bias to respond anti-clockwise of the target (μ = -0.889° ± 1.635°; Figure 2A, inset).

Importantly, there were no significant differences between strong and weak imagers for behavioral precision (Figure 2B; $t_{(38)}$ = -0.965, p = 0.341, two-tailed) or any other of the estimated behavioral parameters (Figure S1). This indicates that the high individual differences in visual imagery were not associated with performance differences in the visual working memory task. We used a Bayesian analysis to assess the evidence for absence of a difference in behavioral precision between the weak and strong imagery groups. The Bayes factor indicated that the data were 2.2 times more likely under the null hypothesis (BF_{01} = 2.239) which provides weak evidence for the absence of an effect of imagery vividness on behavioral precision (Jeffreys, 1998).
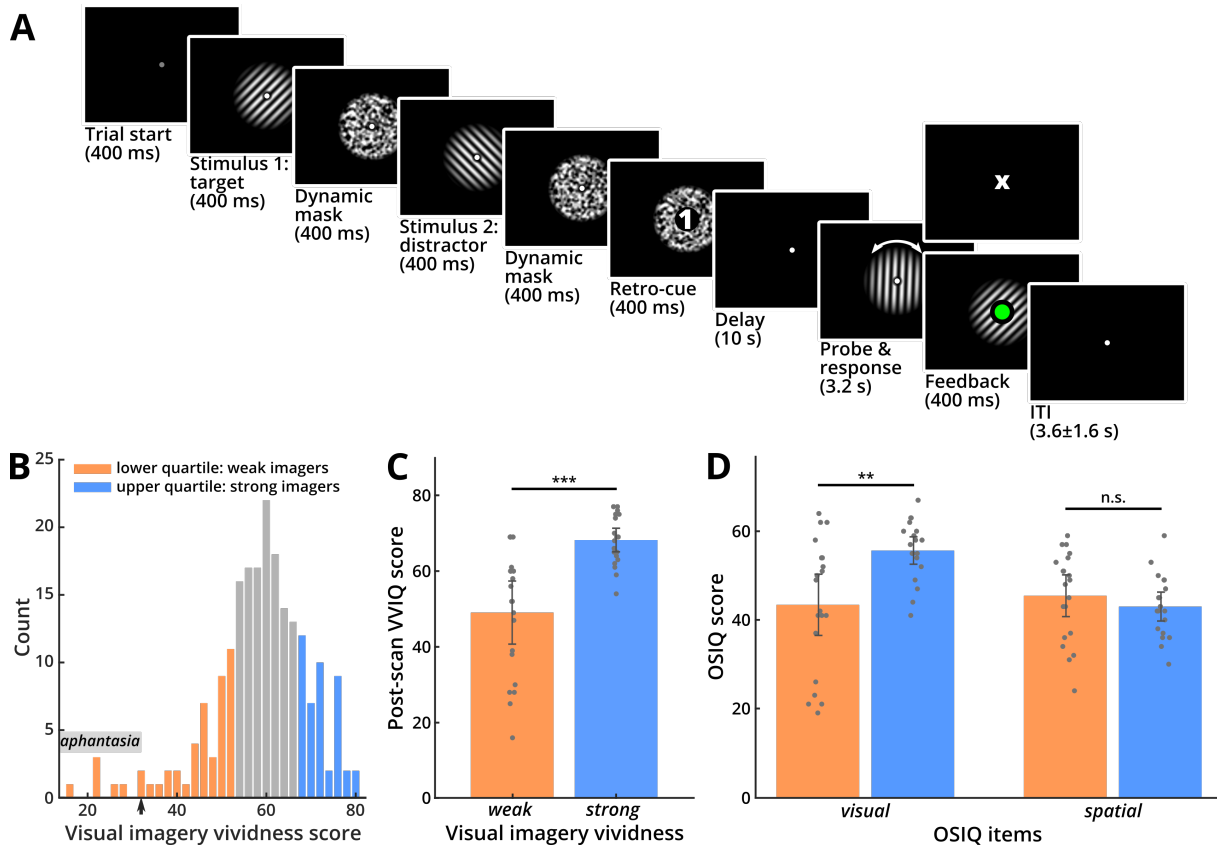
Figure 1. Experimental task and questionnaire data. (A) Sequence of events in one trial of the experiment. In each trial, participants were successively presented with two orientation stimuli, each followed by a dynamic noise mask. Orientations were drawn from a set of 40 discrete, equally spaced orientations between 0° and 180°. The stimuli were followed by a numeric retro-cue ("1" or "2"), indicating which one of them was to be used for the subsequent delayed-estimation task ("target"), and which could be dropped from memory ("distractor"). The orientation of the cued target grating had to be maintained for a 10-second delay. After the delay a probe grating appeared, which had to be adjusted using two buttons and then confirmed via an additional button press. Subsequently, visual feedback was given indicating whether a response was given in time (by turning the fixation point green, lower panel) or missed (by displaying a small "X" at the end of the response period if no response was given in time, upper panel). Cue and feedback are enlarged in this illustration for better visibility. **(B)** Distribution of the scores in an online visual imagery questionnaire (VVIQ, see Methods) that was used for recruitment. Subjects from the upper (blue) versus lower (orange) quartiles of the distribution were recruited for the strong and weak imagery vividness groups, respectively. The small arrow on the x-axis points to the aphantasia cutoff. **(C)** Questionnaire scores of the post-scan (repeated) VVIQ for weak and strong imagers, as defined by the recruitment scores. The post-scan scores of the weak imagery group were significantly lower than those for the strong imagery group, indicating that the groups were consistent across the study and repeated testing ($t_{(38)}$ = -5.086, p < 0.001, two-tailed; error bars: 95 % confidence intervals). **(D)** Results for the visual and spatial items from the OSIQ. Scores for the visual items were significantly lower for weak imagers ($t_{(38)}$ = -3.338, p = 0.002, two-tailed). Scores for the spatial items did not differ between groups ($t_{(38)}$ = 0.895, p = 0.377, two-tailed; error bars: 95 % confidence intervals), as expected from previous work (Bainbridge et al., 2021; Keogh & Pearson, 2018).

5
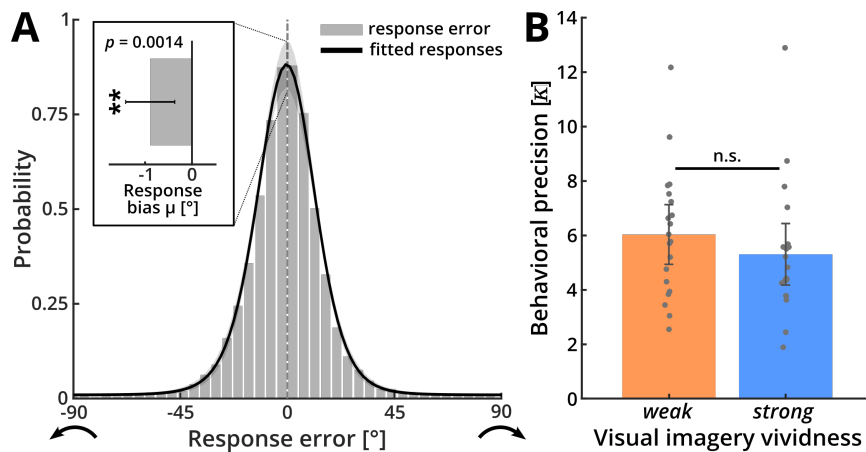
Figure 2. Behavioral results. (A) Histogram of deviations between the reported and the true orientation of the target stimuli (grey bars) and a model fit of behavioral responses across all subjects (black line). For this, the responses were modeled using a von Mises mixture model (vMMM) for detections (responses to target orientations, assumed to follow a von Mises distribution with mean 0° plus bias μ and behavioral precision κ_1), swap errors (false responses to distractor orientations, following the same assumptions as detections) and guesses (assumed to follow a continuous uniform distribution between -90° and +90°). The model estimated individual probabilities for each of these three event classes (resulting in mixture coefficients, r_1, r_2 and r_3, respectively). The estimated parameters indicate that participants accurately performed the task: they correctly responded to the target direction in around 95 % of trials (r_1 = 0.947 ± 0.063). Across participants, responses were precise (κ_1 = 5.673 ± 2.377), with a small but significant bias to respond anti-clockwise of the target (inset; μ = -0.889 ± 1.635°; $t_{(39)}$ = -3.437, p = 0.0014, two-tailed; error bar: 95 % confidence interval). See Figure S1 for details on the other estimated parameters. **(B)** Behavioral precision (κ_1) for strong and weak imagers separately. Behavioral precision did not significantly differ between groups (error bars: 95 % confidence intervals).

Orientation reconstruction from fMRI data

We used a brain-based decoder to reconstruct orientation representations encoded in the patterns of signals in early visual cortex (V1-V3, see Methods). Across all subjects, we were able to reconstruct the true physical target orientation above chance-level for an extended period following delay onset (Figure 3A, green line): At 5 s after delay onset, the accuracy rose to 12 % above chance, where it plateaued until 3 s after probe onset. Following probe onset, the accuracy increased steeply before falling back towards baseline. This later peak in reconstruction performance is likely to reflect the perceptual information of the adjustable probe grating after it had been rotated by the participants to report the target orientation. Reconstruction of the reported orientation yielded a very similar pattern of results (Figure 3A, red line). This close resemblance was expected, given the close match between target and reported orientations (see Figure 2A).

6
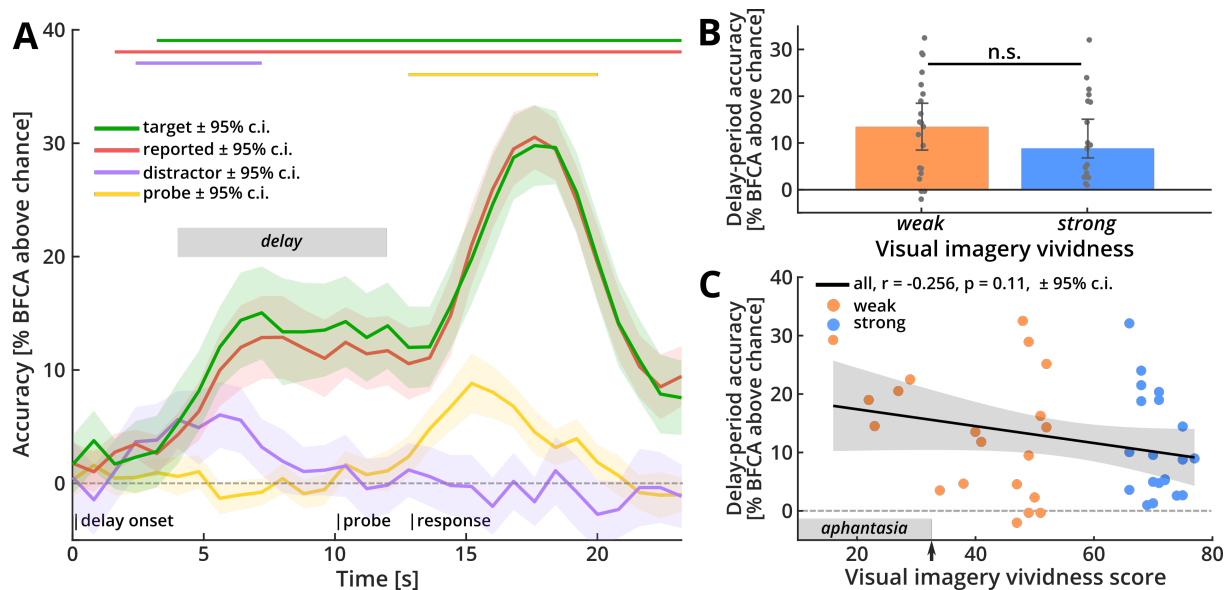
Figure 3. Orientation reconstruction from early visual cortex. (A) Reconstruction performance for orientations based on brain signals from early visual areas V1-V3. The y-axis plots the accuracy (BFCA, see Methods), across time for target (green), reported (red), distractor (purple) and probe (yellow) orientations. The horizontal lines above the graph indicate time periods where this reconstruction was significantly above chance (permutation-based cluster-mass statistic, see Methods). The target orientation (green) could be reconstructed above chance-level throughout the delay and report periods (cluster-p < 0.001). Reconstruction of the reported orientation (red) followed a highly similar pattern (cluster-p < 0.001). The distractor orientation (purple) could only be reconstructed early in the trial (cluster-p < 0.001), before falling back to baseline. Reconstruction of the adjustable probe orientation (yellow) was only possible late in the trial (large cluster: cluster-p < 0.001; small cluster: cluster-p = 0.015), after it had been presented (shaded areas: 95 % confidence intervals). The gray box marks the preregistered delay-period time window used for subsequent analyses. **(B)** Target reconstruction performance for strong and weak imagers separately, pooled across the preregistered delay-period (gray bar in (A)). Delay-period decoding accuracy did not differ between weak and strong imagers ($t_{(38)}$ = 0.821, p = 0.417, two-tailed; error bars: 95 % confidence intervals). **(C)** Detailed correlation between delay-period accuracy (BFCA) and visual imagery score. There was no significant correlation between the strength of delay-period representations and imagery vividness even when using the full graded imagery scores (shaded area: 95 % confidence interval). Neural information during the delay-period was significantly above chance-level even for aphantasic individuals with a visual imagery score below 32 (grey bar at x-axis; $t_{(4)}$ = 8.758, p < 0.001, one-tailed, E.A.). The arrow on the x-axis points to the aphantasia cutoff.

We also conducted several checks to test for other predictions of our analysis. First, we reconstructed the orientation of the distractor, i.e., the task-irrelevant orientation stimulus that was not cued and could thus be forgotten after the retro-cue. As expected, information about this distractor orientation (Figure 3A, purple line) was only present briefly at the beginning of the trial after which the accuracy returned to chance-level for the remainder of the trial. In line with previous work on the representation of task-irrelevant stimuli (Albers et al., 2013; Ester et al., 2013; Harrison & Tong, 2009), this transient early information presumably reflects the perceptual signal following the presentation of the distractor early in the trial, delayed by the hemodynamic lag. Second, we reconstructed the initial random starting orientation of the adjustable probe grating (Figure 3A, yellow line). As expected, this resulted in an informative time window late in the trial, after probe onset, likely reflecting the perceptual signal of the adjustable probe before it was rotated for the behavioral response. Together, this pattern of results indicates the presence of sustained, content-selective representations of the

7

232   memorized stimuli during the delay-period, while task-irrelevant stimulus information was

233   quickly dropped from memory. In an additional analysis we confirmed that the decodable

234   information was not related to systematic eye-movements (Figure S2).

235

236   *Group differences in delay-period representations*

237   Next, we proceeded to address the key question whether there was any indication that strong

238   and weak imagers differed in their memory-related information in early visual cortex. Despite

239   robust group-wise reconstruction performance, reconstruction accuracy did not differ between

240   strong and weak imagers (Figure 3B; $t_{(38)}$ = 0.821, p = 0.417, two-tailed). This was confirmed

241   by a post-hoc Bayesian t-test, which provided moderate evidence in favor of the null hypothesis

242   over our original prediction that the early visual cortex signal of strong imagers should contain

243   more information about the stimulus (BF_{01} = 5.275).

244

245   To further corroborate the effect, we assessed the possibility that the effect of imagery

246   vividness is more gradual in nature and thus might not be captured by the categorical group

247   difference. To address this, we calculated the correlation between delay-period accuracies and

248   graded imagery vividness scores. Again, the result was not significant (Figure 3C; r = -0.256,

249   p = 0.11), with strong evidence for the absence of a positive correlation (BF_{01} = 12.442). There

250   was also no relationship between working memory signals and any of the post-scan imagery

251   assessments (see Table S1). Note that delay-period accuracy was significantly greater than

252   chance-level even for the five participants with a visual imagery score of below 32 (marked

253   with a grey bar on the x-axis of Figure 3C; one-sample t-test: $t_{(4)}$ = 8.758, p < 0.001, one-tailed;

254   E.A.), which is generally considered the threshold for aphantasia (Zeman et al., 2015). Taken

255   together, these results suggest that imagery vividness, at least in the form of subjective

256   questionnaire scores, does not affect the strength of delay-period representations of target

257   orientations in early visual cortex.

258

8
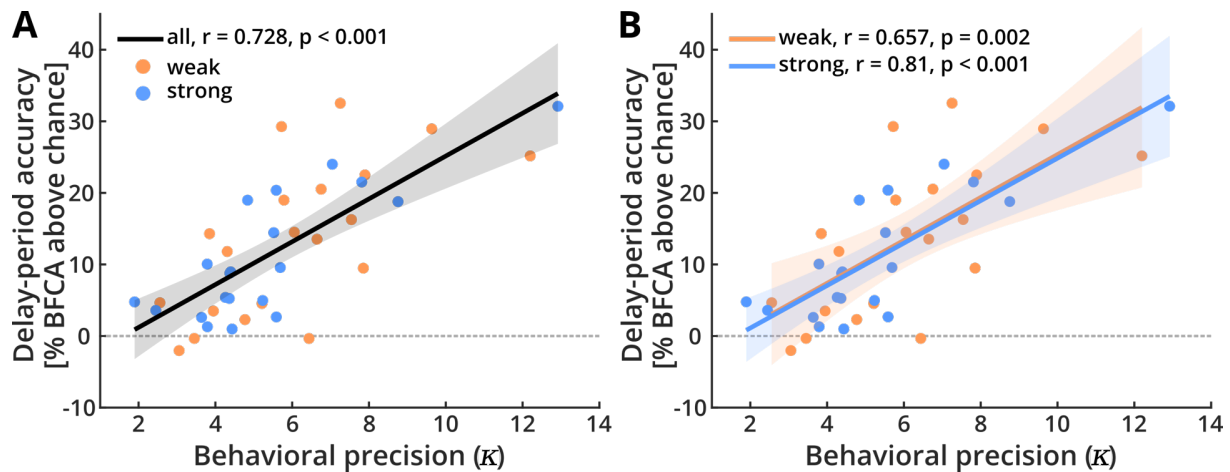
Figure 4. Behavioral precision versus decodable neural information from early visual cortex. Correlation between the behavioral precision (kappa, κ_1) in the task and the accuracy of brain-based reconstruction. The strength of delay-period representations was highly predictable of behavioral precision, both **(A)** across all participants and **(B)** within strong and weak imagery vividness groups. Shaded areas indicate 95 % confidence intervals.

Finally, we tested a further prediction that would be expected if strong imagers relied more on sensory information encoded in early visual cortex than weak imagers. In that case, there should be a tighter predictive link between behavioral performance and the encoding of information in early visual areas, especially for strong imagers. For this, we assessed whether there was more performance-predictive information in early visual areas of strong imagers. In this additional analysis (E.A.) we observed a strong correlation between delay-period accuracy and behavioral precision (Figure 4A; $r = 0.728$, $p < 0.001$), which was the same across groups (Figure 4B; strong: $r = 0.81$, $p < 0.001$; weak: $r = 0.657$, $p = 0.002$). Interestingly, half of the variance in delay-period accuracy could be explained by behavioral precision (R^2, all: 0.53; strong: 0.656; weak: 0.432). This strong effect suggests that the signals in early visual cortex could potentially play a direct role in maintaining the sensory stimulus across the memory delay (as suggested by the sensory recruitment hypothesis), and that this does not depend on whether a person is a strong or a weak imager.

Discussion

In this study, we investigated to which extent an individual's visual imagery vividness affects the strength of working memory representations in their visual cortex. Two experimental groups, strong and weak imagers, performed a visual working memory task, which involved memorizing images of oriented lines over a delay. In both groups we found that early visual cortex contained robust information about the remembered orientations across the entire delay period. Importantly, the level of this information did not differ between strong and weak imagery groups. There was also no apparent dependency of visual cortex representations on any other subjective measure of encoding strategy (see Table S1), suggesting that remembered orientations were encoded equally strongly in the visual areas irrespective of an individual's

9

290   imagery vividness. Crucially, even the five participants with a VVIQ score of below 32, which

291   is generally considered the threshold for complete absence of phenomenal imagery

292   ("aphantasia"; Zeman et al., 2015) showed comparable visual neural information to the strong

293   imagers (see Figure 2C). Our results therefore show that working memory signals can be

294   present in early visual cortex even in the (near) absence of phenomenal imagery.

295

296   While working memory signals in early visual cortex were not modulated by imagery vividness,

297   we did observe a strong correlation between encoded information and individual behavioral

298   precision. Moreover, the overall strength of this effect was also indistinguishable between

299   imagery groups. This suggests that the sensory information represented in early visual cortex

300   was equally important for strong and weak imagers to successfully guide behavior. We thus

301   find no evidence for differences between strong and weak imagers, neither in the encoding of

302   sensory information nor in the degree to which this information is predictive of behavior. These

303   results go against our key prediction from the cognitive-strategies framework of working

304   memory (Pearson & Keogh, 2019), according to which strong imagers should retain higher

305   levels of stimulus information in their early visual cortices during working memory, compared

306   to weak imagers. Our results therefore call into question the importance of experienced

307   imagery vividness in the modulation of early visual cortex recruitment during working memory.

308   Please note that these null effects were based on preregistered analyses and are supported

309   by additional Bayesian analyses.

310

311   To our knowledge, this is the first study to specifically investigate the decodability of working

312   memory representations in the context of individual differences in imagery ability. While some

313   studies have considered the relationship between visual imagery and stimulus decoding

314   (Albers et al., 2013; Dijkstra et al., 2017; Dijkstra et al., 2018), they have relied on random

315   samples of participants, potentially not covering the entire spectrum of imagery ability and not

316   addressing the effects of individual differences. One study found that the overlap between

317   imagery and perception signals in early visual cortex is modulated by trial-by-trial imagery

318   measures (Dijkstra et al., 2017). In a later study, the same authors could successfully cross-

319   decode between the neural signatures of weak and strong imagers, indicating that the

320   decodable signal between both groups was similar (Dijkstra et al., 2018). While the second

321   study in particular seems to support our results, caution is advised when comparing results

322   obtained via trial-by-trial measures of imagery with trait measures such as VVIQ scores.

323   Another study has reported a positive relationship between imagery ability and decoding

324   accuracy (Albers et al., 2013), however, note that the authors of that study equated imagery

325   ability with task performance, making this result more analogous to our reported relationship

326   between target reconstruction and behavioral precision. Therefore, our present finding that

327   working memory signals do not seem to depend on imagery vividness is not in direct
328   contradiction to these previous decoding studies.

330   Importantly, our study was specifically designed to assess the neural encoding of working
331   memory contents, not the neural representations of imagery. If working memory signals in early
332   visual areas were to exclusively reflect imagery, one would predict these working memory
333   signals both to be modulated by imagery ability and to be completely absent for individuals
334   without phenomenal imagery (aphantasics). Our results show that both are not the case.
335   Please note that we are not claiming that visual imagery and visual working memory are never
336   based on the same neural signals. It is possible that imagery in strong imagers recruits the
337   same neural representations that are also used for visual working memory. This would be
338   compatible with findings from previous studies (Albers et al., 2013; Dijkstra. et al., 2017;
339   Dijkstra et al., 2018). However, our finding that even a strong reduction in imagery does not
340   affect the decodable information suggests that these early visual signals are not necessarily
341   tied to imagery. What our data show, is that neural representations of working memory
342   contents are still observable and have a comparable information level even for individuals with
343   weak or absent imagery. Thus, working memory signals can be dissociated from visual
344   imagery in early visual cortex. Note that the current study did not focus on any particular
345   encoding strategy and therefore does not allow any claims about the neural encoding of
346   imagery contents. While it would be interesting to investigate how the strength of imagery
347   representations varies with the vividness of subjectively experienced imagery, this is a
348   question for future research and was not the aim of this study.

350   Our finding of a close link between sensory information in the delay period and behavioral
351   working memory performance is in line with several previous studies (Bettencourt & Xu, 2016;
352   Ester et al., 2013; Hallenbeck et al., 2021; Harrison & Tong, 2009; Iamshchinina et al., 2021).
353   Based on our highly sensitive method for reconstructing continuous stimulus features from
354   voxel patterns, the neural information explained more than half of the between-subject
355   variance in behavioral performance (see Methods for more details), which further corroborates
356   the link between information encoded in early visual cortex and memorization of visual
357   information across brief delays. Additionally, we found that sensory information was retained
358   only for the cued and thus task-relevant stimulus but was not present for the uncued image.
359   These results are in line with sensory recruitment accounts of working memory (D'Esposito &
360   Postle, 2015), or more generally with a multi-level representation of sensory information across
361   delays (Christophel et al., 2017), according to which cortical areas that are used for the
362   encoding of task-relevant sensory information are also recruited for the brief memorization of
363   that information. This task-dependent retention of information in early visual cortex could point

364 towards some form of *active maintenance* throughout the delay after offset of the stimulus.
365 This could be achieved by neural mechanisms such as recurrent processing within early visual
366 cortex (Lamme & Roelfsema, 2000) or by feedback from higher regions (Gazzaley & Nobre,
367 2012) and could include short-term synaptic plasticity (Mongillo et al., 2008; Rose et al., 2016).
368 Please note that sensory recruitment does not make any assumptions about the strategy with
369 which sensory information is encoded, i.e., whether it is accompanied by imagery or not.

370

371 It is worth pointing out that there has been some debate about the importance of early visual
372 cortex for the generation and maintenance of visual imagery in general. For instance, results
373 from activation-based studies have suggested that imagery effects in early visual cortex might
374 be linked to sensory memory retrieval (Kaas et al., 2010). Further, it has been shown that vivid
375 phenomenal imagery can be preserved in cortically blind patients after strokes to occipital
376 areas (Bartolomeo et al., 1998; Chatterjee & Southwood, 1995; de Gelder et al., 2015),
377 indicating that early visual cortex is not essential for visual imagery. Similarly, lesions in
378 temporal regions have been reported to selectively affect visual imagery but leave visual
379 perception largely preserved (Moro et al., 2008; Thorudottir et al., 2020), which has been taken
380 as evidence that visual imagery depends on a temporal network (Spagna et al., 2021).
381 Together, this would suggest a functional dissociation of early visual cortex and visual imagery
382 (Bartolomeo et al., 2020), with imagery relying on higher-level representations beyond early
383 visual cortex (Bartolomeo, 2008). As a consequence, orientation-specific signals could be
384 maintained in early visual cortex, but weak imagers might not be able to access them to
385 produce phenomenal imagery. On this basis, one could speculate that the weak imagers in
386 our case might have had a deficit in a (potentially temporal) imagery network, whereas working
387 memory performance is based on sensory information that is largely intact. Early visual
388 information would thus be available to solve the working memory task but would not
389 necessarily lead to the experience of imagery. Importantly, however, this is at odds with a large
390 body of behavioral, neuroimaging and brain-stimulation work which suggests a close link
391 between signals in early visual areas and imagery (Albers et al., 2013; Dijkstra et al., 2017;
392 Keogh et al., 2020; Pearson, 2019), a discrepancy which will have to be resolved by future
393 research. Another explanation for our results might be that our participants simply did not use
394 visual strategies at all, or just to a small extent. This would be in direct opposition of the
395 cognitive-strategies framework, which assumes a close correspondence between individual
396 imagery ability and the cognitive strategy used to solve a working memory task (Pearson &
397 Keogh, 2019). Strong imagers usually report to use visual strategies (Bainbridge et al., 2021;
398 Keogh et al., 2021; Logie et al., 2011), and the spontaneous use of visual vs. non-visual
399 strategies by strong and weak imagers has also been confirmed behaviorally, by showing that
400 only strong imagers were affected by distracting visual input during a working memory delay

12

401 (Keogh & Pearson, 2014). It is therefore unlikely that the strong imagery group in this study
402 relied predominantly on non-visual strategies to solve the task.

403

404 One reason for some of the discrepancies in the imagery literature may lie in the different ways
405 in which imagery vividness is quantified across studies (Pearson, 2020). To date, various
406 approaches have been suggested, including self-report questionnaires, trial-by-trial vividness
407 measures (Dijkstra et al., 2017; Dijkstra et al., 2018; Dijkstra et al., 2017) and several measures
408 that are related to certain spontaneous perceptual (Pearson et al., 2008) or physiological (Kay
409 et al., 2022) reactions or anatomical features (Bergmann et al., 2016). It is not yet clear,
410 however, which of these measures provides the best approximation for general individual
411 imagery ability. Some of the more objective measures in particular have been used very rarely
412 and still await calibration with respect to more conventional measures of visual imagery. In
413 contrast, the VVIQ provides a well-established, reliable assessment for individual differences
414 in imagery vividness (Dijkstra et al., 2018; Pearson et al., 2011). VVIQ scores have been
415 shown to successfully capture the relationship between imagery vividness and neural signals
416 (Amedi et al., 2005; Cui et al., 2007; Lee et al., 2012), and people are generally able to provide
417 good metacognitive judgments about their own imagery abilities (Pearson et al., 2011;
418 Rademaker & Pearson, 2012). Further, the VVIQ is closely related to a perceptual priming
419 based measure of imagery ability (Pearson et al., 2008, 2011). In combination with pre-
420 selection and high test-retest reliability, the VVIQ scores should therefore provide a reasonably
421 good estimate of general imagery ability in the two groups recruited for this study.

422

423 It is worth mentioning that our reconstruction results might be explained by other factors than
424 orientation-specific visual representations. Please note that in decoding studies it is generally
425 not possible to fully guarantee that information pertains to the features intended by the
426 researcher instead of other latent confounding variables such as spatial attention or motor
427 preparation that co-vary with these features, as we have pointed out previously (Christophel
428 et al., 2017). For example, the distribution of spatial attention can be very different across
429 seemingly homogenous stimulus sets (Liu, 2016; Yun et al., 2013). Thus, when decoding
430 between two object images one might be decoding the spatial distribution of attention rather
431 than the object identity. This could also be the case for the orientation stimuli used here.
432 However, the role of early visual cortex in encoding of orientations as here has long been
433 established both at a cellular level (Hubel & Wiesel, 1968) as well as the population level
434 (Haynes & Rees, 2005; Kamitani & Tong, 2005; Ts'o et al., 1990). Orientation stimuli as here
435 have been used in many cornerstone studies of working memory (Albers et al., 2013; Bae &
436 Luck, 2019; Harrison & Tong, 2009) and imagery (Keogh & Pearson, 2011, 2014; Pearson et
437 al., 2008). Nonetheless, future studies will be needed to test whether all these findings of

13

438 orientation encoding in early visual cortex during working memory generalize to other stimulus

439 sets.

440

441 In conclusion, we show that the active maintenance of stimulus-related information in early

442 visual areas was present also in participants who report a near-absence of visual imagery. The

443 encoding of sensory information and its link to performance was strong and indistinguishable

444 across different levels of imagery. This provides further evidence for the view that the

445 recruitment of early visual cortex for working memory can be dissociated from visual imagery,

446 at least for participants with weak or absent imagery. Thus, informative working memory

447 representations in visual cortex are maintained irrespective of whether a person is able to

448 engage in vivid imagery or not.

449

Acknowledgements

455

Author contributions

457 Conceptualization, S.W., and J.-D.H.; methodology, S.W., T.C., K.G., J.S., and J.-D.H.;

458 investigation, S.W., T.C.; formal analysis, S.W., K.G., and J.-D.H.; software, S.W., K.G., and

459 J.S.; visualization, S.W.; writing, S.W., and J.-D.H.; supervision, J.-D.H.

460

Declaration of interests

462 The authors declare no competing interests.

463

Methods

465 *Data and code availability*

466 Original code, summary statistics describing the reported data and processed datasets which

467 can be used to recreate the figures in this manuscript have been deposited and are publicly

468 available at https://github.com/simonweber91/WM_VI_EVC. Any additional data and

469 information required to reanalyze the data reported in this paper are available from the lead

470 contact upon reasonable request.

471

472 *Preregistration*

473 The main analysis workflow of this study (including custom preprocessing steps, parameter

474 choices, ROIs and newly implemented statistical models) was preregistered at

475 https://osf.io/34y9z. The preregistration was submitted after data acquisition, but prior to data

476 processing and analysis. All preregistered analysis procedures were developed and/or

477 optimized on a separate fMRI dataset from a related study (Barbieri et al., 2023). Please note

478 that we did not change any of the preregistered workflows. However, we did perform additional

479 analyses and performed more extended statistical testing (e.g., Bayesian and permutation-

480 based tests) whenever it proved necessary to the quality of the study. All of these additional

481 analyses are indicated as E.A. ("extended analysis") in this text.

482

483 *Recruitment*

484 Two groups of study participants were preselected for the study using an online version of the

485 Vividness of Visual Imagery Questionnaire (VVIQ; Marks, 1973) The questionnaire was

486 implemented and hosted on the online survey platform SoSci Survey (www.soscisurvey.de)

487 and local respondents were recruited via in-house mailing lists for experimental studies, study

488 participant databases and Facebook. Respondents gave informed consent prior to being

489 directed to the questionnaire and again before providing an email address for recruitment at

490 the end of the questionnaire.

491 We received a total of 263 online responses, 210 of which fulfilled the physiological, medical

492 and demographic criteria for participation in the MRI study. Respondents whose VVIQ scores

493 fell either into the upper or lower quartiles of the response distribution were assigned to the

494 strong and weak imagery groups, respectively, and contacted for participation in the fMRI

495 experiment (Figure 1B). From these groups we recruited a total of 42 fMRI participants. All

496 participants were healthy, right-handed individuals between 18 and 40 years old with no history

497 of neurological or psychiatric disorders. One participant dropped out of the study before

498 completing all scanning sessions. The data of a second participant had to be discarded due to

499 technical issues with the MRI scanner. Therefore, we collected complete datasets of 40

500 participants (female: 23, age: 28.05 ± 6.064 years), 20 each per experimental group (average

501 VVIQ score; weak: 40.75 ± 11.571; strong: 70.7 ± 3.262).

502 Participants gave written informed consent prior to the fMRI experiment. They received

503 monetary compensation of 10€/h for the fMRI sessions and a bonus of 10€ for completion of

504 both scanning sessions. Following April 19, 2021, participants were required to present a

505 negative SARS-CoV-19 rapid test result (not older than 24 hours) before entering the MRI

506 facility. To compensate for the additional effort, we paid an additional 20€ for each SARS-CoV-

507 19 rapid test. The study was approved by the ethics committee of the Humboldt-Universität zu

508 Berlin and conducted according to the principles of the Declaration of Helsinki (World Medical

509 Association, 2013).

510

Stimuli

The experiment was implemented using MATLAB R2018b (The MathWorks, Inc.) and Psychtoolbox 3 (Brainard, 1997; Kleiner et al., 2007). All stimuli were presented on black background, to avoid residual luminance interfering with potential visual imagery during the delay period (Keogh & Pearson, 2014). For stimulation, we used circular high contrast sine-wave Gabor patches with phase 0, contrast 0.8 and a spatial frequency of 0.02 cycles per pixel. Stimuli were presented inside a circular aperture with an inner diameter of 0.71 dva and an outer diameter of 8.47 dva. A white fixation dot of 0.18 dva was placed at the center of the inner aperture (Figure 1A).

The set of target orientations comprised 40 discrete, equally spaced orientations separated by 180°/40 = 4.5°. To avoid the exact cardinal directions (0°, 45°, 90°, 135°), the orientations were slightly shifted by 1.125°, resulting in a set of orientations between 1.125° and 176.625°. Another set of 40 gratings, which served as distractors, was created by shifting the target orientations by 4.5°/2 = 2.25°, yielding orientation stimuli between 3.375° and 178.875°. This ensured that (i) target and distractor orientations were never exactly the same and (ii) both sets of orientations avoided the exact cardinal directions. Since we presented 40 trials in each run (see below), each target and distractor orientation was shown once during each run, in randomized order. Accordingly, target and distractor orientations were counterbalanced across runs. The starting orientation of the probe grating was randomly selected from a uniform distribution between 0° and 180° on each trial.

To avoid afterimages, we used a custom dynamic noise mask (Figure 1A). For each presentation of the mask, we initialized a 42-by-42 array of an equal number of black and white squares. Each time the screen was refreshed (refresh rate: 60 Hz), the array was scrambled along the rows and columns and smoothed by convolving it with a 2 x 2 box blur kernel. This created a highly dynamic noise mask that reliably suppressed afterimages of the high-contrast gratings. Masks were presented inside the same circular aperture as the stimuli.

fMRI task

The visual stimuli were presented on an MRI-compatible monitor (dimensions: 52 x 39 cm, resolution: 1024 x 768 px), positioned at the far end of the scanner bore, and viewed via an eye-tracking compatible mirror mounted on top of the head-coil. The distance between the eyes and the center of the monitor was 158 cm.

Each trial of the experiment started with the presentation of a central fixation dot which remained visible throughout the entire trial (Figure 1A). Participants were instructed to fixate the dot at all times. After 0.4 s, participants were sequentially presented with two gratings (see above), one serving as the target and the other as the distractor. Each grating was shown for 0.4 s, followed by 0.4 s of a dynamic, high-contrast noise mask to avoid after-images. After the

16

548   second mask a numerical retro-cue (0.4 s) was presented at the location of the fixation dot,

549   indicating to the participants to remember the orientation of either the first ("1") or second ("2")

550   grating during the subsequent delay period. The delay period lasted for 10 s, during which only

551   the fixation dot remained visible on the screen. After the delay, a probe grating with random

552   starting orientation appeared for 3.2 s. Participants were asked to adjust the orientation of the

553   probe grating in a way that it corresponded to the remembered (target) orientation, using two

554   buttons with the index and middle fingers of their right hand. After adjustment, participants had

555   to confirm their response by pressing a button with the index finger of their left hand. If the

556   response was completed within the time-window of 3.2 s, the fixation dot turned green for the

557   remainder of the response period as visual feedback. If participants failed to provide a

558   response in time, a small "X" was presented at the location of the fixation dot for 0.4 s. Trials

559   were separated by a variable inter-trial interval (ITI) of 3.6 ± 1.6 s. Participants completed 40

560   trials per run and a total of 8 runs, equally split across 2 fMRI sessions on separate days,

561   resulting in 320 trials per participant.

562

563   *MRI data acquisition*

564   MRI data were collected with a 3-Tesla Siemens Prisma MRI scanner (Siemens, Erlangen,

565   Germany) using a 64-channel head coil. At the beginning of each session, we recorded a high-

566   resolution T1-weighted MPRAGE structural image (208 sagittal slices, TR = 2400 ms, TE =

567   2.22 ms, TI = 1000 ms, flip angle = 8°, voxel size = 0.8 mm^2 isotropic, FOV = 256 mm). On

568   each of the two days, this was followed by four experimental runs, for each of which we

569   recorded a series of 965 T2-weighted functional images using a multi-band accelerated EPI

570   sequence with a multiband factor of 8 (TR = 800 ms, TE = 37 ms, flip angle = 52°, voxel size

571   = 2 mm^2 isotropic, 72 slices, 1.9 mm inter-slice gap), resulting in a duration of 12:52 min per

572   run. The first four TR of each sequence were discarded.

573

574   *Eye-tracking*

575   We used an EyeLink 1000 Plus (SR-Research) eye-tracker to record gaze position and pupil

576   size of the dominant eye of each participant during the experimental runs. The tracker was

577   positioned at the far end of the scanner bore (eye-lens-distance: 85 cm) on a long-distance

578   mount and was calibrated once at the beginning of each session. Due to technical difficulties,

579   we were only able to record eye-tracking data of 26 participants (13 per experimental group).

580

581   *Post-experiment questionnaires*

582   After the second session, participants completed three questionnaires: (i) the Vividness of

583   Visual Imagery Questionnaire (VVIQ, as a post-experimental reference); (ii) the Object–Spatial

584   Imagery Questionnaire (OSIQ; Blajenkova et al., 2006) a 30-item questionnaire probing the

585   strength of visual and spatial imagery; and (iii) a purely heuristic strategy questionnaire, asking

586   (on a 5-point scale) for the degree to which they had used specific mnemonic strategies to

587   remember the target orientations and complete the task, including visual, verbal, spatial,

588   reference to cardinal directions, reference to a clock face, some kind of individual code, or

589   other.

590

591   *Behavioral data analysis*

592   Behavioral responses were modeled by fitting a von Mises mixture model (vMMM) to the

593   distribution of behavioral response errors (see Töpfer et al., 2022; original code available at

594   https://github.com/JoramSoch/RDK_vMMM). The model is inspired by previous work on

595   modelling detections from working memory with similarly continuous features (Zhang & Luck,

596   2008). In our case, we assume that on every trial participants either *detect* the target

597   (responses to target orientations, assumed to follow a von Mises distribution with mean 0° plus

598   bias μ and precision κ), make a *swap error* (responses to distractor orientations, following the

599   same assumptions as detections) or *guess* (assumed to follow a continuous uniform

600   distribution between -90° and +90°). Each of these three potential trial-wise outcomes

601   (detections, swaps and guesses) has an associated probability distribution indicating how

602   probable each potential response angle is, given the orientation of the stimulus (i.e., target and

603   distractor). The overall response distribution is considered a linear combination of these three

604   individual event probability distributions with associated probabilities as mixture coefficients r_1,

605   r_2 and r_3.

606   According to this approach, the probability of observing a specific response evaluates to

607

608   $$P(\theta_r|\theta_t, \theta_d, \vec{r}, \mu, \vec{\kappa}) = P(\text{'detection'}) \cdot P(\theta_r|\text{'detection'}) + P(\text{'swap'}) \cdot P(\theta_r|\text{'swap'}) + P(\text{'guess'}) \cdot P(\theta_r|\text{'guess'})$$

609   $$= r_1 \frac{\exp\left[\kappa_1 \cos((\theta_t - \theta_r)_{\text{circ}} \frac{\pi}{90} - \mu)\right]}{2\pi I_0(\kappa_1)} + r_2 \frac{\exp\left[\kappa_2 \cos((\theta_d - \theta_r)_{\text{circ}} \frac{\pi}{90} - \mu)\right]}{2\pi I_0(\kappa_2)} + r_3 \frac{1}{2\pi}$$

610

611   where θ_r is the reported orientation in degrees; θ_t, θ_d and are the target and distractor

612   orientations in degrees, respectively; $\vec{r}$ is a vector containing r_1, r_2 and r_3, the event

613   probabilities for the three model components (detections, swap errors and guesses); $\vec{\kappa}$ is a

614   vector containing κ_1 and κ_2, the precisions for detections and swap errors, respectively; μ is

615   the response bias and $I_0(\kappa_i)$ is the modified Bessel function of order 0. As κ_1 reflects the width

616   of the response distribution for target detections, we report this parameter as our key measure

617   for behavioral precision.

618

619   *fMRI preprocessing*

620   Processing and analysis of fMRI data was performed in MATLAB 2021b, using SPM12, The

621   Decoding Toolbox (Hebart et al., 2015) and custom scripts (see below). MR images were

622 converted into NIfTI format for further processing. Before the analysis, BOLD images were

623 spatially realigned and resliced. The T1 image of each session was coregistered to the first

624 image of the respective BOLD series. We then calculated normalization parameters to the

625 Montreal Neurological Institute (MNI) standard space. These were used to project probabilistic

626 maps of our regions of interest (ROIs) into the native space of each individual participant to

627 guide voxel selection during the reconstruction analysis (see below). Following realignment,

628 the time series of each voxel's raw data were temporally detrended, to remove slow signal

629 drifts that accumulate across a given run. This was implemented using cubic spline

630 interpolation (modifying an existing algorithm; Tanabe et al., 2002). The time series of voxel

631 data for a given run was separated into 40/2 = 20 segments of equal size. The data from each

632 segment was averaged to create query points (nodes), which were then used for cubic spline

633 interpolation, creating a smooth function modeling the slow signal drifts in the voxel data across

634 the run. The number of nodes was specifically set to half the number of trials per run, to avoid

635 the modeling (and thereby, removal) of within-trial effects. The drift-estimate was then

636 subtracted from the voxel data. This procedure was repeated for every voxel and every run.

637 After detrending, we applied temporal smoothing to the data by running a moving average of

638 width 3 TR across the data of each run.

639 To increase the signal-to-noise ratio for samples from trials with neighboring stimulus

640 orientations, we developed a method that we refer to as "feature-space smoothing". Feature-

641 space smoothing accounts for the assumption that, in a feature-continuous stimulus space,

642 samples that lie closely together in feature space (e.g., neighboring orientations) should

643 produce a similar neural response and therefore a similar voxel signal. By reducing the

644 contribution of noise to the measurements of neighboring samples, it should be possible to

645 increase the amount of information represented in the voxel signal across the feature space.

646 We addressed this issue by using a gaussian smoothing kernel to compute a weighted average

647 of the voxel signal corresponding to a given orientation and its neighbors (Figure S3). This

648 means that samples close to a given orientation in feature space contribute more to the

649 resulting average than those further away. The number (or distance) of samples included in

650 the average is determined by the width (full width at half maximum, FWHM) of the smoothing

651 kernel. Please note that we confirmed through simulations that feature-space smoothing can

652 substantially increase signal-to-noise ratio and thereby reconstruction accuracies without

653 producing spurious above-chance accuracies in the case of null data (Figure S3). In this study,

654 we used nested cross-validation across subjects to determine the optimal kernel width for each

655 participant (see below). Please note that all these approaches for temporal detrending and

656 feature-space smoothing were developed and optimized on a separate dataset (from a related

657 study; Barbieri et al., 2023) and both were pre-registered and checked for artifacts or spurious

658 effects.

19

659

Early visual cortex ROI

660

661 As our goal was to determine the strength of working memory representations in visual sensory

662 stores depending on visual imagery vividness, we restricted our analysis to visually driven

663 voxels in early visual cortex (V1, V2, V3). These regions have been shown repeatedly to

664 similarly encode working memory representations of orientation (and other visual) stimuli

665 (Christophel et al., 2012; Christophel & Haynes, 2014; Harrison & Tong, 2009; Serences et al.,

666 2009). In a first step we combined the probabilistic anatomical maps of V1, V2 and V3 (Wang

667 et al., 2015) to create a combined map in standard space, collapsing across left and right

668 hemispheres. We then transformed this map into the native space of each participant, by

669 applying the inverse normalization parameters estimated during preprocessing. The individual

670 maps were then thresholded at 0.1, to exclude voxels that had a less than 10 % probability of

671 being part of a given area, and binarized. This resulted in an average ROI size of 5938.6 ±

672 858.45 voxels. In a second step we identified visually driven voxels within that ROI. For this,

673 we estimated a GLM with regressors for all trial events (target, distractor, cue, delay and probe,

674 plus 6 head motion realignment parameters as regressors of no interest). Regressors were

675 convolved with a canonical hemodynamic response function. We then calculated a contrast for

676 the target regressor (vs. an implicit baseline), in order to determine voxels with significant

677 activation in response to the target, irrespective of orientation. The resulting statistical

678 parametric maps were then used in combination with the individual anatomical ROIs for voxel

679 selection in the multivariate reconstruction analysis. For this, we selected the voxels rank-

680 ordered by their respective *t*-score (from the unspecific target contrast) within the anatomical

681 ROI for each individual. The cutoff yielding the exact number of voxels used for reconstruction

682 was determined via nested cross-validation across subjects (see below).

683

Orientation reconstruction from fMRI data

684

685 The aim of our reconstruction analysis was to predict the angle of the orientation stimulus from

686 the multivariate signal of the preprocessed raw data in the early visual cortex ROI. Note that

687 the space of orientations is circular between 0° and 180°. To account for this, we implemented

688 periodic support vector regression (pSVR), a periodic extension of the SVR (Drucker et al.,

689 1996). First, we projected the angular labels into a periodic space by calculating two sinusoids

690 in the range [0°, 180°). Both functions had an amplitude of 1 and a period of 180°, so that one

691 period spanned the entire label space. One function was shifted by 45°, so that the combination

692 of both periodic functions coded for the linear label scale (Figure S4). This is the 180°-

693 equivalent to the way sine and cosine functions between 0° and 360° code for the angles on a

694 unit circle.

695   Next, we individually predicted each set of labels from the multivariate voxel pattern using the

696   LIBSVM (Chang & Lin, 2011) implementation of SVR with a non-linear radial basis function

697   (RBF) kernel, via a leave-one-run-out cross-validation. Before prediction, the voxel signals in

698   the training data were rescaled to the range [0, 1]. The scaling parameters were then applied

699   to the test data ("across-scaling"; Hebart et al., 2015).

700   After prediction of both sets of periodic labels $(\widehat{x}_i, \widehat{y}_i)$ we computed the reconstructed angular

701   orientation $\widehat{\theta}_i$ using the four-quadrant inverse tangent:

702

703 $$\widehat{\theta}_i = \mathrm{atan2}(\widehat{x}_i, \widehat{y}_i)$$

704

705   The analysis was repeated for the 30 TRs (24 s) following delay-onset, for each TR individually.

706   This allowed for a time-resolved estimation of how orientations were represented in the visual

707   cortex across the entire trial.

708

709   *Reconstruction performance evaluation*

710   To evaluate the accuracy of the orientation reconstruction, we computed the feature-

711   continuous accuracy (FCA). FCA is a rescaling of the absolute angular deviation (between

712   predicted and true label) into the range 0-100 % and can be calculated, for the case of stimuli

713   that are 180°-periodic, as (Pilly & Seitz, 2009)

714

715 $$\mathrm{FCA}(\theta_i, \widehat{\theta}_i) = \frac{90 - \left|(\theta_i - \widehat{\theta}_i)_{\mathrm{circ}}\right|}{90} * 100$$

716

717   where θ_i is the true orientation in the i-th trial and $\widehat{\theta}_i$ is the associated reconstructed orientation.

718   This trial-wise measure of reconstruction performance can be easily interpreted as a feature-

719   continuous analogue to the accuracy measure of more conventional classification approaches:

720   a value of 100 % means that there is no deviation between true and reconstructed orientations,

721   i.e., perfect reconstruction; 50 % means deviation of 45°, which for circular orientation data is

722   equivalent to guessing and can be considered as the chance-level; and 0 % means that

723   reconstructed and true orientations are exactly orthogonal. FCA can be averaged to quantify

724   reconstruction accuracy across trials.

725   For behavioral responses, the orientation labels may not be uniformly distributed across the

726   orientation space, but clustered around, for example, cardinal axes. In a reconstruction setting,

727   this would be analogous to a classification case with unequal (or unbalanced) numbers of

728   classes, where the predictive model can exploit the uneven distribution of classes to simply

729   predict the more frequent class more often. To account for this potential source of bias, we

730   calculated a balanced FCA (BFCA). BFCA is an extension of the concept of balanced accuracy

21

731   (Brodersen et al., 2010) for continuous variables. It is calculated by computing the integral of

732   the trial-wise FCA from 0° to 180° (i.e., the orientation-space), using trapezoidal numerical

733   integration across the sorted true and reconstructed orientations: (Barbieri et al., 2023)

734

735
$$\text{BFCA} = \frac{1}{180} \int_0^{180} \text{FCA}(\theta, \hat{\theta}) \, d\theta$$

736

737   The process of integration assigns lower weights to the FCA values in the well-populated parts

738   of the label-distribution and higher weights to the less populated parts. Thus, BFCA is a non-

739   trial-wise measure of reconstruction performance, which accounts for the potential bias in FCA

740   caused by non-uniformly distributed labels. We report BFCA as our key measure for

741   reconstruction accuracy. Note that this approach has been previously tested to exclude the

742   possibility of artifactual results.

743

744   *Parameter optimization*

745   As mentioned above, we used an across-subjects nested cross-validation to determine the

746   optimal values of two parameters for each participant individually: (i) the width of the gaussian

747   kernel used for feature-space smoothing, and (ii) the number of voxels entered into the

748   analysis. For (i), we chose FWHM values between 0° (i.e., no smoothing) and 90°, in steps of

749   10°. Thus, we had a set of 10 possible kernel widths for smoothing. For (ii), we chose voxel

750   counts between 250 and 2500, in steps of 250. This resulted in a set of 10 possible voxel

751   counts. To select the specific voxels entered into the analysis, we first masked the individual

752   target-versus-baseline *t*-maps with the warped anatomical ROIs (see above) and then selected

753   the n voxels with the highest *t*-scores within those ROIs, with n representing a number from

754   the set of possible voxel counts. The reconstruction analysis was then run for every

755   combination of FWHM values and voxel counts.

756   After reconstruction, we determined the optimal parameters for each subject in the following

757   way: First, we calculated the mean BFCA across all remaining subjects for every parameter

758   combination, resulting in one value per combination and time point. Second, we averaged

759   across the preregistered delay-period TRs (TRs 6-15 following delay onset), as we were

760   specifically interested in potential group differences during this time window. This yielded one

761   BFCA value per parameter combination, specifically for the entire delay period. The parameter

762   combination that yielded the highest BFCA was then assigned to the left-out subject. This was

763   repeated for every subject and resulted in an average FWHM value of 74.5 ± 9.04 and an

764   average voxel count of 1750 ± 211.83.

765

766

767   *Statistical Testing*

768   As we were specifically interested in potential group differences during the delay-period,

769   statistical testing for differences between the strong and weak imagery groups was based on

770   the time points in the trial which most likely only reflect delay period activity. Since the canonical

771   hemodynamic response has a buildup of ~5 seconds, we considered the TRs 6-15 in the 30

772   TR timeframe that we analyzed, corresponding to a time window of 4 s after delay onset to 2

773   s after probe onset (please note that this time window is 0.4 s shorter than described in the

774   preregistration, as the preregistered time window would have resulted in 10.5 instead of 10

775   TRs). This preregistered time window should avoid the leaking of stimulus- or probe-

776   representations into the delay-period analysis.

777   We used two-tailed two-sample *t*-tests to test for potential differences in the reconstruction

778   scores between the experimental groups. Further, we calculated Pearson's *r* to assess the

779   correlation between outcome variables (E.A.).

780

781   *Cluster-based permutation approach (E.A.)* We were interested at which time points during the

782   trial we could detect significant above-chance reconstruction accuracy. To account for the

783   multiple-comparisons (Groppe et al., 2011) and autocorrelation (Purdon & Weisskoff, 1998)

784   issues that arise for such time-resolved analyses, we adopted a non-parametric cluster-based

785   permutation approach (Bullmore et al., 1999; Groppe et al., 2011; Maris & Oostenveld, 2007).

786   This procedure was performed after the parameter optimization described above, to restrict

787   the time-consuming permutation analysis to one set of parameters per subject. We repeated

788   this approach separately for each reconstructed label type: target, distractor, probe and

789   reported orientation.

790

791   *Bayesian tests (E.A.).* As our results indicated no significant differences between our two

792   groups, we used Bayesian hypothesis tests to assess the evidence for this absence. Bayesian

793   hypothesis tests are used to describe the probability of observing the measured data under

794   the null and alternative hypothesis, respectively (Keysers et al., 2020). This likelihood is

795   quantified using the Bayes factor (BF), a continuous measure of evidence for either hypothesis.

796   Specifically, we used two Bayesian hypothesis tests to assess the evidence for absence of

797   effects: First, in the case of non-significant group-comparisons, we performed follow-up

798   Bayesian independent *t*-tests, using a Cauchy distribution with scale parameter $r = 0.707$ as

799   the prior distribution (Morey & Rouder, 2011). Second, in the case of non-significant

800   correlations, we performed Bayesian correlation with a stretched beta prior of width $\kappa = 1$. All

801   Bayesian hypothesis tests were performed in the open-source software JASP (Love et al.,

802   2019).

803

804   *Orientation reconstruction from eye-tracking data*

805   Participants were instructed to maintain fixation at all times during the experiment. It is at least

806   theoretically conceivable that participants might have used an eye-movement-based strategy

807   to remember target orientations. Eye-movements have also been shown to modulate visual

808   responses in the brain (Merriam et al., 2013). To account for these potentially confounding

809   factors, we investigated whether the gaze position across the trial held information about the

810   target orientation. For this, we subjected the recorded x and y ordinates of 26 participants (for

811   which complete sets of eye-tracking data were available) to the same reconstruction analysis

812   as the fMRI data.

813   Preprocessing of eye-tracking data was performed in MATLAB using functions from the

814   Fieldtrip toolbox (Oostenveld et al., 2011), code adapted from prior work (Urai et al., 2017) and

815   in-house code. Blinks were linearly interpolated and bandpass filtered between 5 Hz (high-

816   pass) and 100 Hz (low-pass). For each trial, we extracted 15 s worth of data following the onset

817   of the first grating. The data from each run was detrended using the same cubic spline

818   interpolation as described above (see Preprocessing of fMRI data). We then downsampled the

819   data by a factor of 10, resulting in 1500 time points per trial.

820   After preprocessing, we entered the data into the same pSVR reconstruction analysis as the

821   fMRI data, using the x and y ordinates of the gaze position as input instead of voxel signal,

822   and evaluated the reconstruction by calculating the BFCA. As with the fMRI data, we tested

823   for clusters of above-chance time points using the cluster-based *t*-mass permutation approach

824   described above.

825

826   *Feature-space smoothing simulation*

827   To demonstrate how feature-space smoothing can increase signal-to-noise ratio (SNR) and

828   increase accuracy in a continuous reconstruction setting, we simulated fMRI data with varying

829   amounts of SNR and used different levels of feature-space smoothing before reconstruction.

830   Following the specifics of our experiment, we simulated data comprising 8 runs with 40 trials

831   each, for 250 voxels. The measured response of voxel i in trial j was generated as

832

833
$$y_{ij} = r_{ij} \cdot s + \varepsilon_{ij}$$

834

835   where r_{ij} is the actual response of voxel i in response to the orientation shown in trial j, s is a

836   scaling factor controlling the ratio of signal and noise, and ε_{ij} is sampled from a standard

837   normal distribution.

838   To simulate the voxel responses, we assumed a population of idealized voxels, where each

839   voxel would exhibit a distinct periodic tuning profile in response to angular orientation. The

840   tuning profile z_i for each voxel i was sampled from a multivariate normal distribution

24

841
$$z_i \sim N(0, K_i)$$

842 where K_i specifies the voxels' periodic covariance kernel. This kernel K_i is given by

843

844
$$K_i(x_m, x_n, \sigma_i) = exp\left[-2\left(\frac{sin\left(\frac{1}{2}(x_m - x_n)\right)}{\sigma_i}\right)^2\right]$$

845

846 where x is a $p \times 1$ vector specifying a grid of possible orientations, such that $x_m, x_n \in [0, 2\pi)$,

847 p is controlling the number of unique, equally spaced values from the feature space; and σ_i is

848 the voxel's unique tuning function smoothness parameter. For this simulation, the smoothness

849 of each voxel was sampled from a gamma distribution: $\sigma_i \sim \Gamma(2,2)$.

850 Thus, voxel- and trial-wise responses could be sampled as

851

852
$$r_{ij} = z_i(\theta_j)$$

853

854 where x_j is the orientation presented during the j-th trial and orientation labels were drawn

855 from a uniform distribution: $\theta_j \sim U(0, 2\pi)$.

856 For the SNR-controlling factor s, we chose 10 values between 0.1 and 1, equally spaced by

857 0.1, as well as 0 (i.e., pure noise). Before reconstruction, we used feature-space smoothing on

858 the data, for FWHM values between 0° (i.e., no smoothing) and 360°, equally spaced by 10°.

859 This resulted in 11 SNR levels and 37 smoothing levels. After pSVR reconstruction, we

860 calculated BFCA as our measure of accuracy. The simulation was repeated 1000 times for

861 each parameter combination. The results of this simulation are summarized in Figure S3.

862

863 **References**

864 Albers, A. M., Kok, P., Toni, I., Dijkerman, H. C., & de Lange, F. P. (2013). Shared

865 Representations for Working Memory and Mental Imagery in Early Visual Cortex.

866 *Current Biology*, *23*(15), 1427–1431. https://doi.org/10.1016/j.cub.2013.05.065

867 Amedi, A., Malach, R., & Pascual-Leone, A. (2005). Negative BOLD Differentiates Visual

868 Imagery and Perception. *Neuron*, *48*(5), 859–872.

869 https://doi.org/10.1016/j.neuron.2005.10.032

870 Bae, G., & Luck, S. J. (2019). What happens to an individual visual working memory

871 representation when it is interrupted? *British Journal of Psychology*, *110*(2), 268–287.

872 https://doi.org/10.1111/bjop.12339

873   Bainbridge, W. A., Pounder, Z., Eardley, A. F., & Baker, C. I. (2021). Quantifying aphantasia
874   through drawing: Those without visual imagery show deficits in object but not spatial
875   memory. *Cortex*, *135*, 159–172. https://doi.org/10.1016/j.cortex.2020.11.014

876   Barbieri, R., Töpfer, F. M., Soch, J., Bogler, C., Sprekeler, H., & Haynes, J.-D. (2023).
877   *Encoding of continuous perceptual choices in human early visual cortex* [Preprint].
878   bioRxiv. https://doi.org/10.1101/2023.02.10.527876

879   Bartolomeo, P. (2008). The neural correlates of visual mental imagery: An ongoing debate.
880   *Cortex*, *44*(2), 107–108. https://doi.org/10.1016/j.cortex.2006.07.001

881   Bartolomeo, P., Bachoud-Lévi, A.-C., De Gelder, B., Denes, G., Dalla Barba, G., Brugières,
882   P., & Degos, J.-D. (1998). Multiple-domain dissociation between impaired visual
883   perception and preserved mental imagery in a patient with bilateral extrastriate lesions.
884   *Neuropsychologia*, *36*(3), 239–249. https://doi.org/10.1016/S0028-3932(97)00103-6

885   Bartolomeo, P., Hajhajate, D., Liu, J., & Spagna, A. (2020). Assessing the causal role of early
886   visual areas in visual mental imagery. *Nature Reviews Neuroscience*, *21*, 2.
887   https://doi.org/10.1038/s41583-020-0348-5

888   Bergmann, J., Genç, E., Kohler, A., Singer, W., & Pearson, J. (2016). Smaller Primary Visual
889   Cortex Is Associated with Stronger, but Less Precise Mental Imagery. *Cerebral Cortex*,
890   *26*(9), 3838–3850. https://doi.org/10.1093/cercor/bhv186

891   Bettencourt, K. C., & Xu, Y. (2016). Decoding the content of visual short-term memory under
892   distraction in occipital and parietal areas. *Nature Neuroscience*, *19*(1), 150–157.
893   https://doi.org/10.1038/nn.4174

894   Blajenkova, O., Kozhevnikov, M., & Motes, M. A. (2006). Object-spatial imagery: A new self-
895   report imagery questionnaire. *Applied Cognitive Psychology*, *20*(2), 239–263.
896   https://doi.org/10.1002/acp.1182

897   Brainard, D. H. (1997). The Psychophysics Toolbox. *Spatial Vision*, *10*(4), 433–436.
898   https://doi.org/10.1163/156856897X00357

899   Brodersen, K. H., Ong, C. S., Stephan, K. E., & Buhmann, J. M. (2010). The Balanced
900   Accuracy and Its Posterior Distribution. *2010 20th International Conference on Pattern
901   Recognition*, 3121–3124. https://doi.org/10.1109/ICPR.2010.764

902   Bullmore, E. T., Suckling, J., Overmeyer, S., Rabe-Hesketh, S., Taylor, E., & Brammer, M. J.
903   (1999). Global, voxel, and cluster tests, by theory and permutation, for a difference
904   between two groups of structural MR images of the brain. *IEEE Transactions on
905   Medical Imaging*, *18*(1), 32–42. https://doi.org/10.1109/42.750253

906   Chang, C.-C., & Lin, C.-J. (2011). LIBSVM: A library for support vector machines. *ACM
907   Transactions on Intelligent Systems and Technology*, *2*(3), 1–27.
908   https://doi.org/10.1145/1961189.1961199

909 Chatterjee, A., & Southwood, M. H. (1995). Cortical blindness and visual imagery. *Neurology*,
910   *45*(12), 2189–2195. https://doi.org/10.1212/WNL.45.12.2189

911 Christophel, T. B., & Haynes, J.-D. (2014). Decoding complex flow-field patterns in visual
912   working memory. *NeuroImage*, *91*, 43–51.
913   https://doi.org/10.1016/j.neuroimage.2014.01.025

914 Christophel, T. B., Hebart, M. N., & Haynes, J.-D. (2012). Decoding the Contents of Visual
915   Short-Term Memory from Human Visual and Parietal Cortex. *The Journal of*
916   *Neuroscience*, *32*(38), 12983–12989. https://doi.org/10.1523/JNEUROSCI.0184-
917   12.2012

918 Christophel, T. B., Klink, P. C., Spitzer, B., Roelfsema, P. R., & Haynes, J.-D. (2017). The
919   Distributed Nature of Working Memory. *Trends in Cognitive Sciences*, *21*(2), 111–124.
920   https://doi.org/10.1016/j.tics.2016.12.007

921 Cichy, R. M., Heinzle, J., & Haynes, J.-D. (2012). Imagery and Perception Share Cortical
922   Representations of Content and Location. *Cerebral Cortex*, *22*(2), 372–380.
923   https://doi.org/10.1093/cercor/bhr106

924 Cui, X., Jeter, C. B., Yang, D., Montague, P. R., & Eagleman, D. M. (2007). Vividness of mental
925   imagery: Individual variability can be measured objectively. *Vision Research*, *47*(4),
926   474–478. https://doi.org/10.1016/j.visres.2006.11.013

927 de Gelder, B., Tamietto, M., Pegna, A. J., & Van den Stock, J. (2015). Visual imagery
928   influences brain responses to visual stimulation in bilateral cortical blindness. *Cortex*,
929   *72*, 15–26. https://doi.org/10.1016/j.cortex.2014.11.009

930 D'Esposito, M., & Postle, B. R. (2015). The Cognitive Neuroscience of Working Memory.
931   *Annual Review of Psychology*, *66*(1), 115–142. https://doi.org/10.1146/annurev-psych-
932   010814-015031

933 Dijkstra, N., Bosch, S. E., & van Gerven, M. A. J. (2017). Vividness of Visual Imagery Depends
934   on the Neural Overlap with Perception in Visual Areas. *The Journal of Neuroscience*,
935   *37*(5), 1367–1373. https://doi.org/10.1523/JNEUROSCI.3022-16.2016

936 Dijkstra, N., Bosch, S. E., & van Gerven, M. A. J. (2019). Shared Neural Mechanisms of Visual
937   Perception and Imagery. *Trends in Cognitive Sciences*, *23*(5), 423–434.
938   https://doi.org/10.1016/j.tics.2019.02.004

939 Dijkstra, N., Mostert, P., Lange, F. P. de, Bosch, S., & van Gerven, M. A. (2018). Differential
940   temporal dynamics during visual imagery and perception. *ELife*, *7*, e33904.
941   https://doi.org/10.7554/eLife.33904

942 Dijkstra, N., Zeidman, P., Ondobaka, S., van Gerven, M. A. J., & Friston, K. (2017). Distinct
943   Top-down and Bottom-up Brain Connectivity During Visual Perception and Imagery.
944   *Scientific Reports*, *7*(1), 5677. https://doi.org/10.1038/s41598-017-05888-8

945 Drucker, H., Burges, C. J. C., Kaufman, L., Smola, A. J., & Vapnik, V. (1996). Support Vector
946   Regression Machines. *Advances in Neural Information Processing Systems*, *9*.

947 Ester, E. F., Anderson, D. E., Serences, J. T., & Awh, E. (2013). A Neural Measure of Precision
948   in Visual Working Memory. *Journal of Cognitive Neuroscience*, *25*(5), 754–761.
949   https://doi.org/10.1162/jocn_a_00357

950 Ester, E. F., Serences, J. T., & Awh, E. (2009). Spatially Global Representations in Human
951   Primary Visual Cortex during Working Memory Maintenance. *Journal of Neuroscience*,
952   *29*(48), 15258–15265. https://doi.org/10.1523/JNEUROSCI.4388-09.2009

953 Gazzaley, A., & Nobre, A. C. (2012). Top-down modulation: Bridging selective attention and
954   working memory. *Trends in Cognitive Sciences*, *16*(2), 129–135.
955   https://doi.org/10.1016/j.tics.2011.11.014

956 Groppe, D. M., Urbach, T. P., & Kutas, M. (2011). Mass univariate analysis of event-related
957   brain potentials/fields I: A critical tutorial review. *Psychophysiology*, *48*(12), 1711–1725.
958   https://doi.org/10.1111/j.1469-8986.2011.01273.x

959 Hallenbeck, G. E., Sprague, T. C., Rahmati, M., Sreenivasan, K. K., & Curtis, C. E. (2021).
960   Working memory representations in visual cortex mediate distraction effects. *Nature
961   Communications*, *12*(1), 4714. https://doi.org/10.1038/s41467-021-24973-1

962 Harrison, S. A., & Tong, F. (2009). Decoding reveals the contents of visual working memory in
963   early visual areas. *Nature*, *458*(7238), 632–635. https://doi.org/10.1038/nature07832

964 Haynes, J.-D., & Rees, G. (2005). Predicting the orientation of invisible stimuli from activity in
965   human primary visual cortex. *Nature Neuroscience*, *8*(5), 686–691.
966   https://doi.org/10.1038/nn1445

967 Hebart, M. N., Görgen, K., & Haynes, J.-D. (2015). The Decoding Toolbox (TDT): A versatile
968   software package for multivariate analyses of functional imaging data. *Frontiers in
969   Neuroinformatics*, *8*, 88. https://doi.org/10.3389/fninf.2014.00088

970 Hubel, D. H., & Wiesel, T. N. (1968). Receptive fields and functional architecture of monkey
971   striate cortex. *The Journal of Physiology*, *195*(1), 215–243.
972   https://doi.org/10.1113/jphysiol.1968.sp008455

973 Iamshchinina, P., Christophel, T. B., Gayet, S., & Rademaker, R. L. (2021). Essential
974   considerations for exploring visual working memory storage in the human brain. *Visual
975   Cognition*, *29*(7), 425–436. https://doi.org/10.1080/13506285.2021.1915902

976 Jacobs, C., Schwarzkopf, D. S., & Silvanto, J. (2018). Visual working memory performance in
977   aphantasia. *Cortex*, *105*, 61–73. https://doi.org/10.1016/j.cortex.2017.10.014

978 Jeffreys, H. (1998). *The theory of probability*. OUP Oxford.

979 Kaas, A., Weigelt, S., Roebroeck, A., Kohler, A., & Muckli, L. (2010). Imagery of a moving
980   object: The role of occipital cortex and human MT/V5+. *NeuroImage*, *49*(1), 794–804.
981   https://doi.org/10.1016/j.neuroimage.2009.07.055

982   Kamitani, Y., & Tong, F. (2005). Decoding the visual and subjective contents of the human
983   brain. *Nature Neuroscience*, *8*(5), 679–685. https://doi.org/10.1038/nn1444

984   Kay, L., Keogh, R., Andrillon, T., & Pearson, J. (2022). The pupillary light response as a
985   physiological index of aphantasia, sensory and phenomenological imagery strength.
986   *ELife*, *11*, e72484. https://doi.org/10.7554/eLife.72484

987   Keogh, R., Bergmann, J., & Pearson, J. (2020). Cortical excitability controls the strength of
988   mental imagery. *ELife*, *9*, e50232. https://doi.org/10.7554/eLife.50232

989   Keogh, R., & Pearson, J. (2011). Mental Imagery and Visual Working Memory. *PLoS ONE*,
990   *6*(12), e29221. https://doi.org/10.1371/journal.pone.0029221

991   Keogh, R., & Pearson, J. (2014). The sensory strength of voluntary visual imagery predicts
992   visual working memory capacity. *Journal of Vision*, *14*(12), 7–7.
993   https://doi.org/10.1167/14.12.7

994   Keogh, R., & Pearson, J. (2018). The blind mind: No sensory visual imagery in aphantasia.
995   *Cortex*, *105*, 53–60. https://doi.org/10.1016/j.cortex.2017.10.012

996   Keogh, R., Wicken, M., & Pearson, J. (2021). Visual working memory in aphantasia: Retained
997   accuracy and capacity with a different strategy. *Cortex*, *143*, 237–253.
998   https://doi.org/10.1016/j.cortex.2021.07.012

999   Keysers, C., Gazzola, V., & Wagenmakers, E.-J. (2020). Using Bayes factor hypothesis testing
1000   in neuroscience to establish evidence of absence. *Nature Neuroscience*, *23*(7), 788–
1001   799. https://doi.org/10.1038/s41593-020-0660-4

1002   Klein, I., Dubois, J., Mangin, J.-F., Kherif, F., Flandin, G., Poline, J.-B., Denis, M., Kosslyn, S.
1003   M., & Le Bihan, D. (2004). Retinotopic organization of visual mental images as revealed
1004   by functional magnetic resonance imaging. *Cognitive Brain Research*, *22*(1), 26–31.
1005   https://doi.org/10.1016/j.cogbrainres.2004.07.006

1006   Kleiner, M., Brainard, D., & Pelli, D. (2007). What's new in Psychtoolbox-3? *Perception*, *36*.

1007   Kosslyn, S. M., Ganis, G., & Thompson, W. L. (2001). Neural foundations of imagery. *Nature
1008   Reviews Neuroscience*, *2*(9), 635–642. https://doi.org/10.1038/35090055

1009   Kosslyn, S. M., & Thompson, W. L. (2003). When is early visual cortex activated during visual
1010   mental imagery? *Psychological Bulletin*, *129*(5), 723–746.
1011   https://doi.org/10.1037/0033-2909.129.5.723

1012   Lamme, V. A. F., & Roelfsema, P. R. (2000). The distinct modes of vision offered by
1013   feedforward and recurrent processing. *Trends in Neurosciences*, *23*(11), 571–579.
1014   https://doi.org/10.1016/S0166-2236(00)01657-X

1015   Lee, S.-H., & Baker, C. I. (2016). Multi-Voxel Decoding and the Topography of Maintained
1016   Information During Visual Working Memory. *Frontiers in Systems Neuroscience*, *10*.
1017   https://doi.org/10.3389/fnsys.2016.00002

Lee, S.-H., Kravitz, D. J., & Baker, C. I. (2012). Disentangling visual imagery and perception of real-world objects. *NeuroImage*, *59*(4), 4064–4073. https://doi.org/10.1016/j.neuroimage.2011.10.055

Lee, S.-H., Kravitz, D. J., & Baker, C. I. (2013). Goal-dependent dissociation of visual and prefrontal cortices during working memory. *Nature Neuroscience*, *16*(8), 997–999. https://doi.org/10.1038/nn.3452

Liu, T. (2016). Neural representation of object-specific attentional priority. *NeuroImage*, *129*, 15–24. https://doi.org/10.1016/j.neuroimage.2016.01.034

Logie, R. H., Pernet, C. R., Buonocore, A., & Sala, S. D. (2011). Low and high imagers activate networks differentially in mental rotation. *Neuropsychologia*, *49*(11), 3071–3077. https://doi.org/10.1016/j.neuropsychologia.2011.07.011

Love, J., Selker, R., Marsman, M., Jamil, T., Dropmann, D., Verhagen, J., Ly, A., Gronau, Q. F., Smíra, M., Epskamp, S., Matzke, D., Wild, A., Knight, P., Rouder, J. N., Morey, R. D., & Wagenmakers, E.-J. (2019). JASP : Graphical Statistical Software for Common Statistical Designs. *Journal of Statistical Software*, *88*(2). https://doi.org/10.18637/jss.v088.i02

Maris, E., & Oostenveld, R. (2007). Nonparametric statistical testing of EEG- and MEG-data. *Journal of Neuroscience Methods*, *164*(1), 177–190. https://doi.org/10.1016/j.jneumeth.2007.03.024

Marks, D. F. (1973). Visual Imagery Differences In The Recall Of Pictures. *British Journal of Psychology*, *64*(1), 17–24. https://doi.org/10.1111/j.2044-8295.1973.tb01322.x

Mechelli, A. (2004). Where Bottom-up Meets Top-down: Neuronal Interactions during Perception and Imagery. *Cerebral Cortex*, *14*(11), 1256–1265. https://doi.org/10.1093/cercor/bhh087

Merriam, E. P., Gardner, J. L., Movshon, J. A., & Heeger, D. J. (2013). Modulation of Visual Responses by Gaze Direction in Human Visual Cortex. *Journal of Neuroscience*, *33*(24), 9879–9889. https://doi.org/10.1523/JNEUROSCI.0500-12.2013

Mongillo, G., Barak, O., & Tsodyks, M. (2008). Synaptic Theory of Working Memory. *Science*, *319*(5869), 1543–1546. https://doi.org/10.1126/science.1150769

Morey, R. D., & Rouder, J. N. (2011). Bayes factor approaches for testing interval null hypotheses. *Psychological Methods*, *16*(4), 406–419. https://doi.org/10.1037/a0024377

Moro, V., Berlucchi, G., Lerch, J., Tomaiuolo, F., & Aglioti, S. M. (2008). Selective deficit of mental visual imagery with intact primary visual cortex and visual perception. *Cortex*, *44*(2), 109–118. https://doi.org/10.1016/j.cortex.2006.06.004

1053   Naselaris, T., Olman, C. A., Stansbury, D. E., Ugurbil, K., & Gallant, J. L. (2015). A voxel-wise
1054   encoding model for early visual areas decodes mental images of remembered scenes.
1055   *NeuroImage*, *105*, 215–228. https://doi.org/10.1016/j.neuroimage.2014.10.018

1056   Oostenveld, R., Fries, P., Maris, E., & Schoffelen, J.-M. (2011). FieldTrip: Open Source
1057   Software for Advanced Analysis of MEG, EEG, and Invasive Electrophysiological Data.
1058   *Computational Intelligence and Neuroscience*, *2011*, 1–9.
1059   https://doi.org/10.1155/2011/156869

1060   Pearson, J. (2019). The human imagination: The cognitive neuroscience of visual mental
1061   imagery. *Nature Reviews Neuroscience*, *20*(10), 624–634.
1062   https://doi.org/10.1038/s41583-019-0202-9

1063   Pearson, J. (2020). Reply to: Assessing the causal role of early visual areas in visual mental
1064   imagery. *Nature Reviews Neuroscience*, *21*, 2. https://doi.org/10.1038/s41583-020-
1065   0349-4

1066   Pearson, J., Clifford, C. W. G., & Tong, F. (2008). The Functional Impact of Mental Imagery on
1067   Conscious Perception. *Current Biology*, *18*(13), 982–986.
1068   https://doi.org/10.1016/j.cub.2008.05.048

1069   Pearson, J., & Keogh, R. (2019). Redefining Visual Working Memory: A Cognitive-Strategy,
1070   Brain-Region Approach. *Current Directions in Psychological Science*, *28*(3), 266–273.
1071   https://doi.org/10.1177/0963721419835210

1072   Pearson, J., & Kosslyn, S. M. (2015). The heterogeneity of mental representation: Ending the
1073   imagery debate. *Proceedings of the National Academy of Sciences*, *112*(33), 10089–
1074   10092. https://doi.org/10.1073/pnas.1504933112

1075   Pearson, J., Rademaker, R. L., & Tong, F. (2011). Evaluating the Mind's Eye: The
1076   Metacognition of Visual Imagery. *Psychological Science*, *22*(12), 1535–1542.
1077   https://doi.org/10.1177/0956797611417134

1078   Pilly, P. K., & Seitz, A. R. (2009). What a difference a parameter makes: A psychophysical
1079   comparison of random dot motion algorithms. *Vision Research*, *49*(13), 1599–1612.
1080   https://doi.org/10.1016/j.visres.2009.03.019

1081   Purdon, P. L., & Weisskoff, R. M. (1998). Effect of temporal autocorrelation due to physiological
1082   noise and stimulus paradigm on voxel-level false-positive rates in fMRI. *Human Brain*
1083   *Mapping*, *6*(4), 239–249. https://doi.org/10.1002/(SICI)1097-0193(1998)6:4<239::AID-
1084   HBM4>3.0.CO;2-4

1085   Rademaker, R. L., & Pearson, J. (2012). Training Visual Imagery: Improvements of
1086   Metacognition, but not Imagery Strength. *Frontiers in Psychology*, *3*.
1087   https://doi.org/10.3389/fpsyg.2012.00224

1088   Ragni, F., Tucciarelli, R., Andersson, P., & Lingnau, A. (2020). Decoding stimulus identity in
1089   occipital, parietal and inferotemporal cortices during visual mental imagery. *Cortex*,
1090   *127*, 371–387. https://doi.org/10.1016/j.cortex.2020.02.020

1091   Reddy, L., Tsuchiya, N., & Serre, T. (2010). Reading the mind's eye: Decoding category
1092   information during mental imagery. *NeuroImage*, *50*(2), 818–825.
1093   https://doi.org/10.1016/j.neuroimage.2009.11.084

1094   Rose, N. S., LaRocque, J. J., Riggall, A. C., Gosseries, O., Starrett, M. J., Meyering, E. E., &
1095   Postle, B. R. (2016). Reactivation of latent working memories with transcranial
1096   magnetic stimulation. *Science*, *354*(6316), 1136–1139.
1097   https://doi.org/10.1126/science.aah7011

1098   Senden, M., Emmerling, T. C., van Hoof, R., Frost, M. A., & Goebel, R. (2019). Reconstructing
1099   imagined letters from early visual cortex reveals tight topographic correspondence
1100   between visual mental imagery and perception. *Brain Structure and Function*, *224*(3),
1101   1167–1183. https://doi.org/10.1007/s00429-019-01828-6

1102   Serences, J., Saproo, S., Scolari, M., Ho, T., & Muftuler, L. (2009). Estimating the influence of
1103   attention on population codes in human visual cortex using voxel-based tuning
1104   functions. *NeuroImage*, *44*(1), 223–231.
1105   https://doi.org/10.1016/j.neuroimage.2008.07.043

1106   Serences, J. T. (2016). Neural mechanisms of information storage in visual short-term
1107   memory. *Vision Research*, *128*, 53–67. https://doi.org/10.1016/j.visres.2016.09.010

1108   Serences, J. T., Ester, E. F., Vogel, E. K., & Awh, E. (2009). Stimulus-Specific Delay Activity
1109   in Human Primary Visual Cortex. *Psychological Science*, *20*(2), 207–214.
1110   https://doi.org/10.1111/j.1467-9280.2009.02276.x

1111   Spagna, A., Hajhajate, D., Liu, J., & Bartolomeo, P. (2021). Visual mental imagery engages
1112   the left fusiform gyrus, but not the early visual cortex: A meta-analysis of neuroimaging
1113   evidence. *Neuroscience & Biobehavioral Reviews*, *122*, 201–217.
1114   https://doi.org/10.1016/j.neubiorev.2020.12.029

1115   Sreenivasan, K. K., Curtis, C. E., & D'Esposito, M. (2014). Revisiting the role of persistent
1116   neural activity during working memory. *Trends in Cognitive Sciences*, *18*(2), 82–89.
1117   https://doi.org/10.1016/j.tics.2013.12.001

1118   Tanabe, J., Miller, D., Tregellas, J., Freedman, R., & Meyer, F. G. (2002). Comparison of
1119   Detrending Methods for Optimal fMRI Preprocessing. *NeuroImage*, *15*(4), 902–907.
1120   https://doi.org/10.1006/nimg.2002.1053

1121   Teng, C., & Kravitz, D. J. (2019). Visual working memory directly alters perception. *Nature*
1122   *Human Behaviour*, *3*(8), 827–836. https://doi.org/10.1038/s41562-019-0640-4

1123 Thorudottir, S., Sigurdardottir, H. M., Rice, G. E., Kerry, S. J., Robotham, R. J., Leff, A. P., &
1124   Starrfelt, R. (2020). The Architect Who Lost the Ability to Imagine: The Cerebral Basis
1125   of Visual Imagery. *Brain Sciences*, *10*(2), 59. https://doi.org/10.3390/brainsci10020059

1126 Tong, F. (2013). Imagery and visual working memory: One and the same? *Trends in Cognitive*
1127   *Sciences*, *17*(10), 489–490. https://doi.org/10.1016/j.tics.2013.08.005

1128 Töpfer, F. M., Barbieri, R., Sexton, C. M., Wang, X., Soch, J., Bogler, C., & Haynes, J.-D.
1129   (2022). Psychophysics and computational modeling of feature-continuous motion
1130   perception. *Journal of Vision*, *22*(11), 16. https://doi.org/10.1167/jov.22.11.16

1131 Ts'o, D. Y., Frostig, R. D., Lieke, E. E., & Grinvald, A. (1990). Functional Organization of
1132   Primate Visual Cortex Revealed by High Resolution Optical Imaging. *Science*,
1133   *249*(4967), 417–420. https://doi.org/10.1126/science.2165630

1134 Urai, A. E., Braun, A., & Donner, T. H. (2017). Pupil-linked arousal is driven by decision
1135   uncertainty and alters serial choice bias. *Nature Communications*, *8*(1), 14637.
1136   https://doi.org/10.1038/ncomms14637

1137 Wang, L., Mruczek, R. E. B., Arcaro, M. J., & Kastner, S. (2015). Probabilistic Maps of Visual
1138   Topography in Human Cortex. *Cerebral Cortex*, *25*(10), 3911–3931.
1139   https://doi.org/10.1093/cercor/bhu277

1140 Yun, K., Peng, Y., Samaras, D., Zelinsky, G. J., & Berg, T. L. (2013). Exploring the role of gaze
1141   behavior and object detection in scene understanding. *Frontiers in Psychology*, *4*.
1142   https://doi.org/10.3389/fpsyg.2013.00917

1143 Zeman, A., Dewar, M., & Della Sala, S. (2015). Lives without imagery – Congenital aphantasia.
1144   *Cortex*, *73*, 378–380. https://doi.org/10.1016/j.cortex.2015.05.019

1145 Zeman, A. Z. J., Della Sala, S., Torrens, L. A., Gountouna, V.-E., McGonigle, D. J., & Logie,
1146   R. H. (2010). Loss of imagery phenomenology with intact visuo-spatial task
1147   performance: A case of 'blind imagination.' *Neuropsychologia*, *48*(1), 145–155.
1148   https://doi.org/10.1016/j.neuropsychologia.2009.08.024

1149 Zhang, W., & Luck, S. J. (2008). Discrete fixed-resolution representations in visual working
1150   memory. *Nature*, *453*(7192), 233–235. https://doi.org/10.1038/nature06860

1151
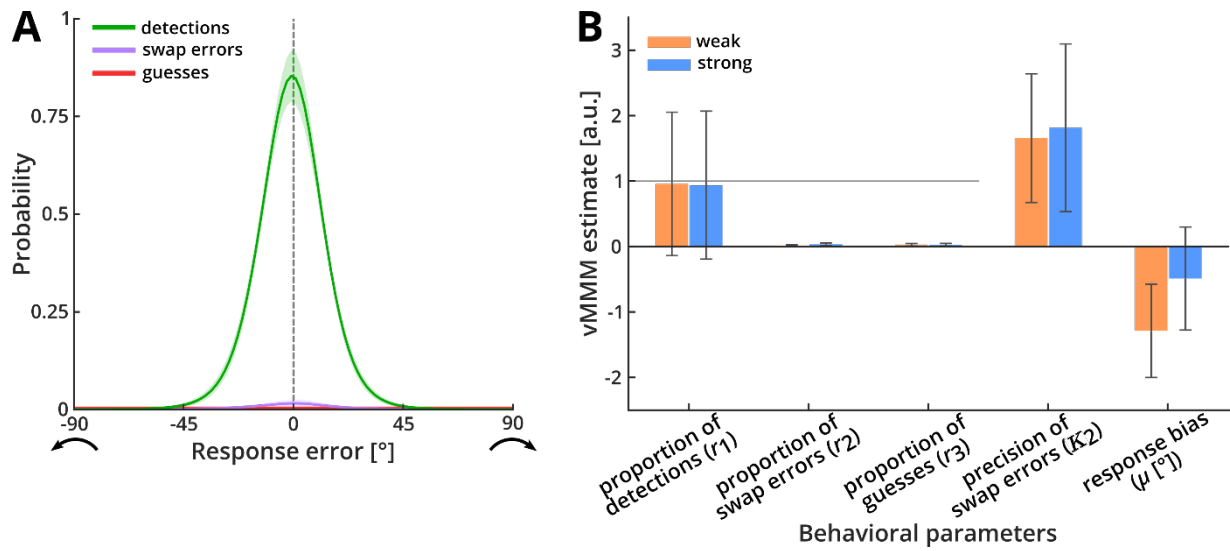
Supplemental Information

Figure S1. Von Mises mixture model (vMMM) fit of behavioral responses. (A) The distribution of behavioral responses was modeled as a combination of the three model components: detections (responses to target orientations, assumed to follow a von Mises distribution with mean 0° plus bias μ and precision κ; green), swap errors (responses to distractor orientations, following the same assumptions as detections; purple) and guesses (assumed to follow a continuous uniform distribution between -90° and +90°; red). These components were weighted by individual event probabilities (mixture coefficients) r_1, r_2 and r_3, respectively. Participants correctly responded to the target direction in 94.7 % of trials (r_1 = 0.947 ± 0.063), and only infrequently made swap errors (r_2 = 0.026 ± 0.034) or guesses (r_3 = 0.027 ± 0.041). Responses to targets were precise (κ_1 = 5.673 ± 2.377), while responses to the distractor, where present, were imprecise (κ_2 = 1.735 ± 2.41). There was a small but significant bias to respond anti-clockwise of the target (μ = -0.889 ± 1.635°; $t_{(39)}$ = -3.437, p = 0.0014, two-tailed; see also Figure 1C). **(B)** Estimated vMMM parameters for strong and weak imagers separately. There was no significant difference between the two groups for any of the estimated parameters (r_1: $t_{(38)}$ = -0.925, p = 0.361; r_2: $t_{(38)}$ = 1.585, p = 0.121; r_3: $t_{(38)}$ = 0.108, p = 0.914; κ_2: $t_{(38)}$ = -0.207, p = 0.837; μ: $t_{(38)}$ = 1.574, p = 0.124, all two-tailed; see Figure 1D for κ_1).
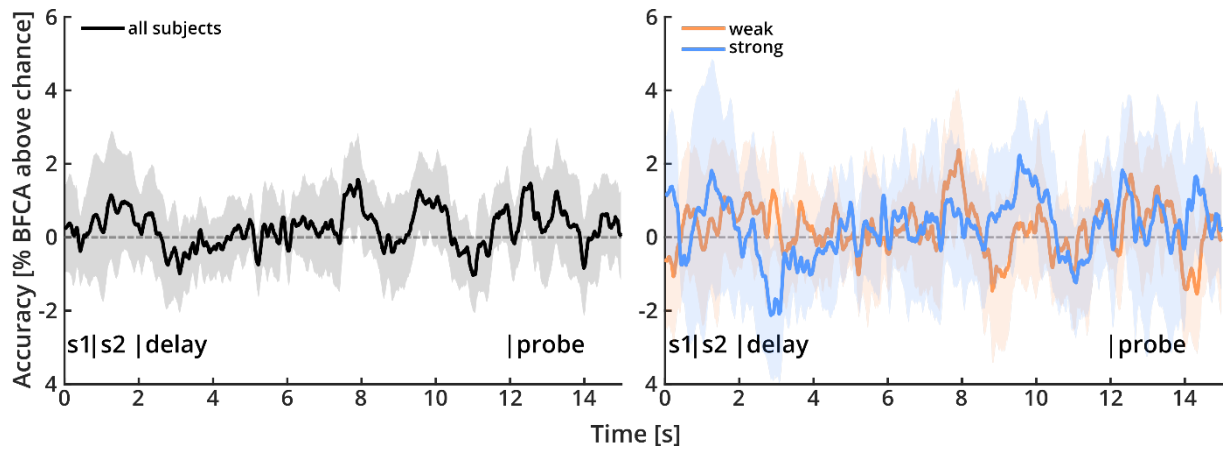
Figure S2. Target reconstruction from eye-tracking data. Reconstruction of target orientation from gaze position across the trial, for all subjects (left panel) and separated by groups (right panel). There were no temporal clusters with significantly above-chance BFCA, suggesting that participants did not systematically use gaze position to maintain target orientation across the delay period. Shaded areas indicate 95 % confidence intervals.
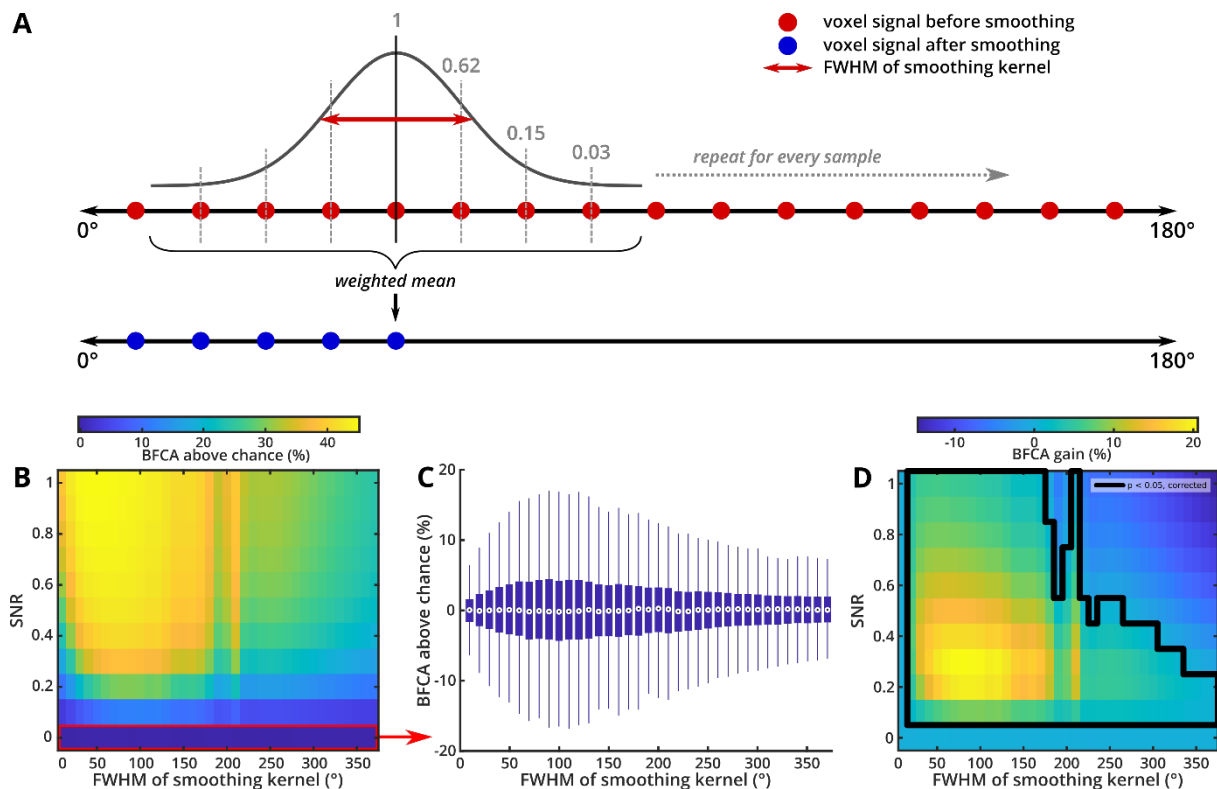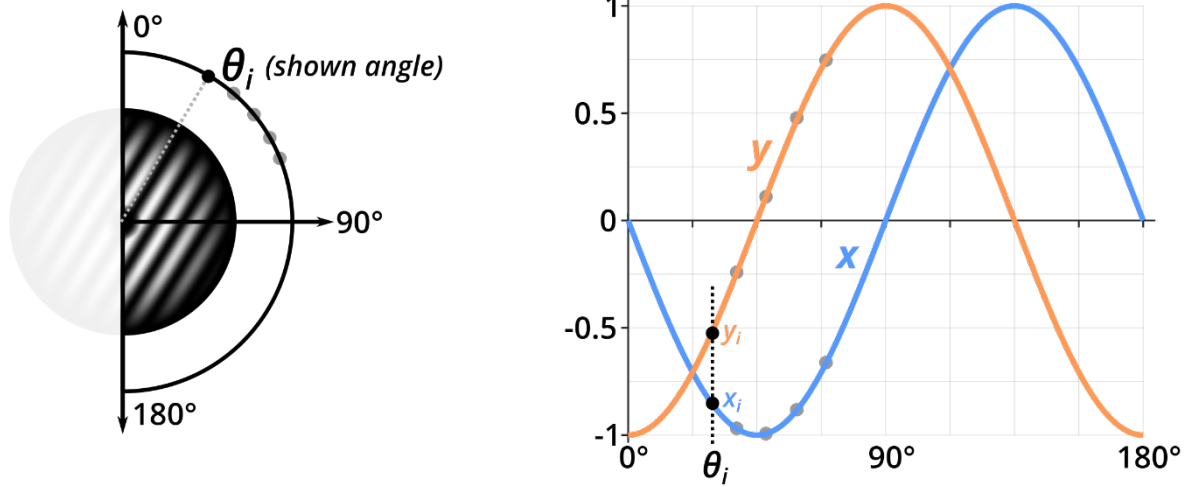
Figure S3. Schematic representation of feature-space smoothing and simulation results. (A) We used a Gaussian smoothing kernel to compute a weighted average from the voxel signal of samples lying closely together in feature space. Samples close to a given orientation in feature-space therefore contribute more to the resulting average than those further away. The full width at half maximum (FWHM) of the smoothing kernel controls the smoothing range, i.e., the number (or distance) of samples that are included in the weighted average. We used FWHM values between 0° (no smoothing) and 90° in steps of 10° and determined the optimal kernel width for each participant via nested cross-validation across subjects. Note that this was done (a) at the level of the input data to the analysis, not the results, (b) for training and test data separately, and (c) was confirmed not to produce artifacts or spurious results by extensive simulations (see (C) and Extended Methods). **(B)** We simulated data with varying levels of SNR and used feature-space smoothing with different kernel widths (measured as FWHM in degrees) before reconstruction of the underlying signal. The plot shows BFCA for all parameter combinations, averaged across 1000 repetitions. **(C)** BFCA across smoothing levels, for the pure noise condition. BFCA remained at chance-level across all levels of smoothing (all $p > 0.25$) and BFCA for any smoothing condition did not differ from the no-smoothing condition (all $p > 0.15$). **(D)** BFCA gain compared to no smoothing, averaged across all 1000 repetitions. The first column corresponds to baseline, i.e., zero smoothing. In the signal conditions ($SNR > 0$), feature-space smoothing was able to reliably increase BFCA compared to no smoothing. The effect was strongest for smoothing kernel widths between 30° and 170°, where we observed increases in accuracy of up to 20 %. Generally, the effect of feature space smoothing was stronger for data with low SNR (orange-yellow area). In cases of extremely high kernel-width and comparatively high SNR (i.e., $SNR > 0.6$ and $FWHM > 220$°), feature-space smoothing had a detrimental effect, meaning that BFCA was decreased compared to no smoothing (dark blue area). Please note, however, that kernel-widths this high do not make any sense for real-world applications and were only included for the purpose of demonstration. We conclude that feature-space smoothing is a powerful preprocessing technique to increase SNR in a feature-continuous reconstruction setting. As the optimal kernel-width for smoothing depends on the specific data and SNR, we recommend using nested cross-validation to determine the optimal FWHM value, similar to the approach described in the main text.
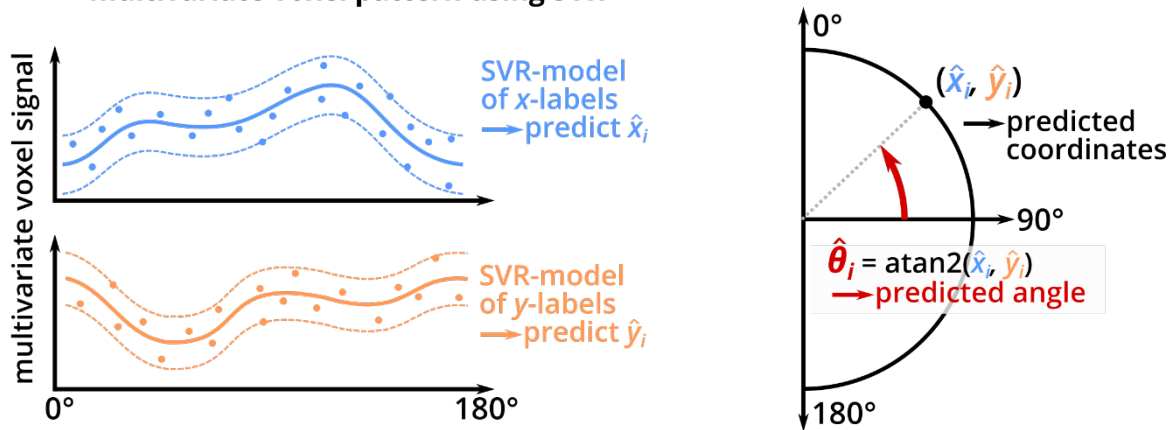
Figure S4. Schematic representation of periodic support vector regression (pSVR). The aim of our reconstruction analysis was to predict an angular label between 0° and 180° from the multivariate voxel signal in response to a stimulus grating with the respective orientation. However, the linear scale of orientation labels (from 0° to 180°) does not reflect the periodic nature of the stimulus (i.e., 0° and 180° are identical). To account for this, we projected the angular labels into a periodic space by fitting two sinusoids into the range [0, 180). Both functions had an amplitude of 1 and a period of 180°, so that one period spanned the entire label space. One function was shifted by 45°, so that the combination of both periodic functions coded for the linear label scale. This is equivalent to the way sine and cosine functions between 0 and 360° code for the angles on a unit circle. We trained and tested a multivariate SVR model for both periodic label sets (x, y) separately. From the combination of the predicted periodic labels, we then reconstructed a predicted angular label using the four-quadrant inverse tangent. The predicted orientation was then compared to the true orientation to derive BFCA, our measure of reconstruction accuracy.

Table S1: Correlation table of all variables of interest (and strategy questionnaire).

	BFCA target	Behav. precision	Pre-scan VVIQ	Post-scan VVIQ	OSIQ visual	OSIQ spatial	Strat. visual	Strat. verbal	Strat. spatial	Strat. cardinal	Strat. clock	Strat. code	Strat. other
BFCA target		0.728***	-0.256	-0.277	-0.297	0.166	-0.203	0.245	-0.289	-0.146	0.173	-0.174	0.402*
Behav. precision	0.728***		-0.127	-0.062	-0.158	-0.011	-0.118	0.274	-0.179	-0.268	0.044	0.061	0.235
Pre-scan VVIQ	-0.256	-0.127		0.867***	0.706***	-0.271	0.109	-0.182	0.073	0.293	0.06	-0.011	-0.43**
Post-scan VVIQ	-0.277	-0.062	0.867***		0.837***	-0.25	0.157	-0.208	0.005	0.246	0.114	0.029	-0.488**
OSIQ visual	-0.297	-0.158	0.706***	0.837***		-0.239	0.273	-0.319*	0.004	0.241	0.089	0.067	-0.564***
OSIQ spatial	0.166	-0.011	-0.271	-0.25	-0.239		-0.011	0.006	0.125	0.128	-0.238	-0.21	0.28
Strat. visual	-0.203	-0.118	0.109	0.157	0.273	-0.011		-0.427**	-0.271	-0.371*	-0.119	-0.233	-0.365*
Strat. verbal	0.245	0.274	-0.182	-0.208	-0.319*	0.006	-0.427**		-0.009	-0.023	-0.316*	0.064	0.14
Strat. spatial	-0.289	-0.179	0.073	0.005	0.004	0.125	-0.271	-0.009		0.195	-0.436**	0.032	-0.051
Strat. cardinal	-0.146	-0.268	0.293	0.246	0.241	0.128	-0.371*	-0.023	0.195		-0.247	-0.01	-0.077
Strat. clock	0.173	0.044	0.06	0.114	0.089	-0.238	-0.119	-0.316*	-0.436**	-0.247		-0.15	-0.144
Strat. code	-0.174	0.061	-0.011	0.029	0.067	-0.21	-0.233	0.064	0.032	-0.01	-0.15		-0.21
Strat. other	0.402*	0.235	-0.43**	-0.488**	-0.564***	0.28	-0.365*	0.14	-0.051	-0.077	-0.144	-0.21	

Table of correlation coefficients between all variables of interest, including the items from the heuristic strategy questionnaire. There are two notable sets of relationships: the strong correlation between target reconstruction accuracy ("BFCA target") and behavioral precision ("Behav. precision"), and the close relationship between pre- and post-scan VVIQ (i.e., test-retest reliability) and the visual OSIQ scores. There are some significant effects between several variables and items from the strategy ("Strat.") questionnaire. Please note, however, that these questions were purely heuristic in nature. We only asked for each strategy in rater general terms and did not ask for the vividness of each strategy. The questions were not based on any previously validated procedure, in contrast to the established VVIQ and OSIQ scales. Also, the ratings on these items have high variance, rendering any interpretation difficult. We are currently not aware of any established and standardized sets of questions regarding the use of cognitive strategies.

Table S2: Descriptive statistics for all variables of interest (and strategy questionnaire).

	BFCA target	Behav. precision	Pre-scan VVIQ	Post-scan VVIQ	OSIQ visual	OSIQ spatial	Strat. visual	Strat. verbal	Strat. spatial	Strat. cardinal	Strat. clock	Strat. code	Strat. other
Mean	12.21	5.673	55.725	58.25	49.525	44.225	0.285	0.141	0.189	0.071	0.186	0.054	0.073
Standard deviation	9.768	2.377	17.332	15.834	12.878	8.636	0.217	0.13	0.119	0.115	0.179	0.092	0.121
Skewness	0.484	1.143	-0.641	-1.055	-1.048	-0.187	1.664	0.453	0.062	1.758	0.435	1.335	1.407
Kurtosis (excess)	-0.862	1.519	-0.708	0.264	0.226	-0.658	3.727	-0.8	-0.066	3.108	-0.93	0.154	0.576

Table of mean, standard deviation, skewness and excess kurtosis for all variables of interest, including the items from the heuristic strategy questionnaire.